Spring 2007

In vitro feasibility testing of floating light-activated minroelectrical stimulators

Ammar Riad Abdo
New Jersey Institute of Technology

ABSTRACT

IN VITRO FEASIBILITY TESTING OF FLOATING LIGHT-ACTIVATED MICROELECTRICAL STIMULATORS

by
Ammar Riad Abdo

One of the major challenges of neural stimulation is the mechanical stress and resulting trauma induced on the implanted electrodes by the constant movement of the interconnects. A potential way of eliminating interconnects is to use floating micro-stimulators that can be activated through optical means. As a method of energy transfer to the micro-stimulator, we propose to use a laser beam at near infrared (NIR) wavelengths.

There are two main objectives in this project to test the feasibility of the main approach; investigate the charge injection capacity of titanium nitride (TiN) and iridium oxide (IrOx) as potential contact materials, and measure the transmitted light power through the neural tissue for various implantation depths. The charge injection capacity of TiN electrodes for an extended range of cathodic voltages was also investigated.

Because the microstimulator will be implanted into the neural tissue, the laser beam must penetrate a few millimeters before reaching the device. The transmitted light power was measured for various types of neural tissue. The transmitted light power through rat brain gray matter was much higher than that of the white matter and the sciatic nerve. Penetration depth and reflectance were calculated according to Lambert-Beer's law from measurements of transmission for various tissue thicknesses.

The results suggest that FLAMES approach is feasible for implantation depths of a few millimeters in the peripheral and central nervous system. Both IrOx and TiN allow sufficient charge injection for this application. TiN is preferred for future experimentation

since TiN does not require a bias voltage to achieve useful charge injection rates, and thus is a good choice as an electrode material in this application.

IN VITRO FEASIBILITY TESTING OF FLOATING LIGHT-ACTIVATED MICROELECTRICAL STIMULATORS

by
Ammar Riad Abdo

A Thesis
Submitted to the Faculty of
New Jersey Institute of Technology
in Partial Fulfillment of the Requirements for the Degree of
Master of Science in Biomedical Engineering

Department of Biomedical Engineering

May 2007

APPROVAL PAGE

IN VITRO FEASIBILITY TESTING OF FLOATING LIGHT-ACTIVATED MICROELECTRICAL STIMULATORS

Ammar Riad Abdo

Dr. Mesut Sahin, Thesis Advisor — Date
Assistant Professor of Biomedical Engineering, NJIT

Dr. Tara Alvarez, Committee Member — Date
Associate Professor of Biomedical Engineering, NJIT

Dr. Bryan Pfister, Committee Member — Date
Assistant Professor of Biomedical Engineering, NJIT

BIOGRAPHICAL SKETCH

Author: Ammar Riad Abdo

Degree: Master of Science

Date: May 2007

Undergraduate and Graduate Education:

- Master of Science in Biomedical Engineering,
  New Jersey Institute of Technology, Newark, NJ, 2007

- Bachelor of Science in Biomedical Engineering,
  The Hashemite University, Zarqa, Jordan, 2004

Major: Biomedical Engineering

In the name of Allah, Most Gracious, Most Merciful

"Are those who know equal to who know not"
(Quran 39:9)

To my parents, to my sister Eiman and to my brother Zaid

ACKNOWLEDGMENT

I would like to express my deepest appreciation to Dr. Mesut Sahin for his supervision, advice, and guidance from the very early stage of this research, and for giving me the chance to work in the Neural Interface Laboratory. I would also like to thank Dr. Tara Alvarez and Dr. Bryan Pfister for being my committee members. Many of my fellow graduate students in the Neural Interface Laboratory are deserving of recognition for their support. This study was supported by a grant from National Institute of Health (1-R21-NS 050757-01A1).

TABLE OF CONTENTS

TABLE OF CONTENTS
(Continued)

Chapter **Page**

LIST OF TABLES

LIST OF FIGURES

Figure **Page**

Figure **Page**

CHAPTER 1

INTRODUCTION

Electrical stimulation is currently used as a treatment method in a number of disorders of the central and peripheral nervous system and is being investigated for many new applications [1]. Many of these applications demand very localized activation of the neural tissue at multiple sites to produce functional changes in the neural activity. In order to achieve this high spatial selectivity, microelectrodes with multiple shanks that are penetrating into the neural tissue have been developed [2]. One of the major challenges of chronically implanted electrodes with penetrating shanks is the mechanical stress and the resulting chronic tissue response induced by the movement of the electrode and the tethering of interconnects. This tethering problem can be solved by replacing the interconnects with telemetry, both for powering the device and controlling the stimulus parameters.

An example of such a wireless, floating device in the peripheral nervous system is the BION® stimulator that is controlled by radio-frequency magnetic waves [3]. Because the telemetry and power circuitry are incorporated into this stimulator, the smallest device size is in the order of several millimeters and therefore it is only suitable for activation of peripheral nerves and muscles. To achieve the level of spatial selectivity needed especially in the central nervous system applications, the device needs to be in the submillimeter range and be able to inject sufficient current for neural stimulation.

As potential way of eliminating interconnects- we introduced a floating light activated micro electrical stimulator (FLAMES) for neural stimulation. As a method of

energy transfer to the micro-stimulator, we used a laser beam at near infrared (NIR) wavelengths.

This project has two main objectives to test the feasibility of the main approach; (1) investigate the charge injection capacity of titanium nitride (TiN) and iridium oxide (IrOx) as a potential contact material of the FLAMES. Platinum (Pt) electrodes have been used in different kind of medical stimulation applications. However, Pt electrodes generate insufficient charges for intracortical or intraspinal stimulation. TiN and IrOx electrodes have been introduced as alternative materials for platinum (Pt). Charge injection capacity measurements were obtained. Various input stimuli were proposed as alternative to the rectangular waveform. We investigate the behavior of the charge as a function of pulse width. Charge injection capacity of TiN electrodes for an extended voltage range was investigated in this work, and (2) measure the transmitted light power through the neural tissues. Because the microstimulator is implanted inside the neural tissue, light must penetrate a few millimeters through the tissue before reaching the diode. We therefore measured the transmitted light power through the neural tissues to measure how deep the FLAMES can be implanted into the peripheral and central nervous system and still be activated. Penetration depth and reflectance were obtained according to Beer's law from measurements of transmission. Rat sciatic nerve, white brain matter, and grey brain matter were investigated in this work.

The future work will involve *in vivo* testing of the FLAMES. The NIR threshold for activation will be measured for a range of pulse widths and the strength duration curve (figure 1.1) will be obtained for various thicknesses of the neural tissue. The voltage field generated by a microstimulator in a volume conductor will be analyzed. The

two major questions to be addressed are: 1. How small can a floating stimulator be made without sacrificing the stimulation strength? 2. How deep can it be implanted into the CNS and still be activated without exceeding the NIR safety exposure limits on the surface?

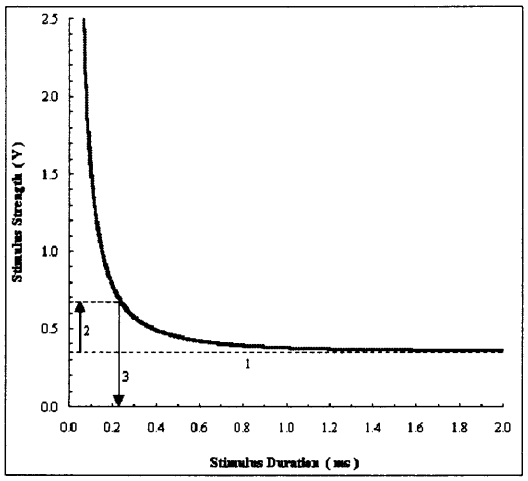

Figure 1.1 Strength-duration curve; a graph relating the intensity of an electrical stimulus its duration for threshold activation.

The thesis includes two main chapters. The first one is the charge injection capacity measurements of titanium nitride and iridium oxide, and the second one is the optical properties of rat neural tissues. The first chapter starts with concepts and theories, and then talks about various groups that contribute in this field. Finally, the chapter describes our work. We introduced various waveforms as input stimuli for electrical stimulation applications. We investigated the charge injection capacity of TiN electrodes for an extended cathodic voltage range as well.

The second chapter begins with theoretical background, and then discussing the background research in this field. Finally, the chapter discusses our work. We studied the

optical properties of rat neural tissues. We measured the transmitted light power through various neural tissues. We calculated the penetration depth and the reflectance according to Beer's law.

CHAPTER 2

CHARGE INJECTION CAPACITY OF TITANIUM NITRIDE AND IRIDIUM OXIDE

2.1 Introduction

Electrical stimulation of nerve cells has been widely used in different medical applications; including the clinical treatment for various medical conditions. The largest clinical success has been achieved in the cochlear implant. The implantable devices have common design constrains including low power consumption, small size, and the ability to stimulate effectively and safely. One of the vital areas where a device can be optimized to satisfy these requirements is the stimulating electrode material [5].

In order to increase selectivity and accommodating more electrodes on the arrays the size of electrodes should be small. This is very important to achieve high resolutions for neural recording and stimulation. Several factors determine the size of the electrodes and the amount of stimulus current that must be produced; the efficiency with which the electrical charge can be transferred from metal to tissue, the electrode impedance, and the stimulating electrode material [4], [5].

A key issue in this kind of applications is the safety requirement, in which an electrode must be able to supply high-density electrical charge without generating irreversible electrochemical reactions. There are two mechanisms for the flow of ionic charges in the biological tissue; the capacitive mechanism and the faradic mechanism. The capacitive mechanism of charge injection involves alternate attraction and repulsion of ions in the tissue in response to the charging and discharging of the electrode double layer. In this mechanism, there is no charge transfer across the electrode-electrolyte

interface, and thus no electrochemical reactions can occur in the interface [4].

The Faradic mechanism involves electron transfer across the electrode-tissue interface and can be divided into reversible and irreversible chemical reactions. The reversible chemical reactions involve species that remain bound to the electrode surface, and therefore these reactions produce no chemical species in the solution that could affect the biological tissues. However, the irreversible reactions produce species that escape from the electrode surface into the surrounding fluid, and therefore these reactions affect the biological tissues by producing metal corrosion or dissolution, gas evolution, or introduction of toxic products. The reversibility of the electrochemical reaction mainly depends on the electrodes material.

There is an operational limit for an electrode, in which there is a limit to the charge that can be injected in either anodic or cathodic direction with reversible surface processes. This is known as "reversible charge injection limit" and expressed as a charge density referred to the real or geometric surface area of the electrode. The current must be reversed before reaching this charge limit to insure chemical reversibility.

Then reversible charge injection limit is quantified by determining the potential limits for water electrolysis which is called the "water window". A water window is the electrical/voltage potential range defined by hydrogen evolution at cathode and oxygen evolution or surface oxidation at anode. This reaction is the most common electrochemical reactions during pulse stimulation, which causes limitation to the charge injection capacity of an electrode.

Theoretically, we can avoid water electrolysis with evolution of hydrogen or oxygen as long as the electrode potential remains between 0.0V versus RHE (reversible

hydrogen electrode) and 1.23V versus RHE. However, it is better to determine the water window limits experimentally because practically there may be considerable over-potential for these reactions. Cyclic voltammetry is a useful technique for this purpose.

"Only a limited number of electrode materials are suitable for chronic stimulation at charge levels greater than 0.15mC/ cm^2" [7]. Threshold charge required for stimulation is variance depends on the medical stimulation application. Table 2.1 shows the Charge injection requirements for electrodes in the CNS based primarily on threshold measurements. Capacitor electrodes which inject charge entirely by capacitive charging and discharging of the electrical double-layer are attractive because they avoid any irreversible reactions that might degrade either the electrode or the surrounding tissue. However, the available charge per unit area is small (~20mC/cm^2 at 1 V). Porous electrodes and dielectric films, such as Ta_2O_5 or TiO_2, are used to increase the charge capacity to physiologically useful levels, however with using these electrodes the charge injection capacity has not been enough for small area (400-2000μm^2) intracortical electrodes at charge and current densities necessary for stimulation [7].

Table 2.1 Charge Injection Requirements for Stimulation

Application	Species	Site	Threshold Charge	Pulse Width
Vision	rabbit	Epi-retinal	0.8-5.7 mC/cm^2	0.1 ms
Vision	human	Epi-retinal	0.16-70 mC/cm^2	2 ms
Vision	human	Epi-retinal	0.8-4.8 mC/cm^2	not reported
Vision	human	Intracortical	2-20 mC/cm^2	0.2 ms
Vision	human	Intracortical	0.2-2.5 mC/cm^2	0.2 ms
Hearing	cat	VCN	0.06-0.09 mC/cm^2	0.15 ms
Micturition	cat	Intraspinal	4 mC/cm^2 (effective)	0.1 ms

Note: Ref [7].

TiN electrodes (capacitive electrodes based on titanium nitride deposited as a highly porous coating by sputter deposition) have been evaluated for neural stimulation applications. These electrodes have relatively large area (>1 mm^2) and modest charge injection densities about 0.5mC/cm^2 with a pulse width of >0.5ms. TiN electrodes are comparable with those required for intracortical stimulation. These electrodes are delivered over longer pulse widths and lower current densities. Furthermore, it is commonly used in the integrated circuit fabrication process, so there is no need for special methods for material deposition [7].

Noble electrodes are faradic electrodes that transfer charge by surface reduction and oxidation of the monolayer oxide film. Platinum electrodes (as one of the noble electrodes) have been widely used in different stimulation applications, including cardiac pacing, and deep brain stimulation. On the other hand, platinum (Pt) electrodes and the other noble electrodes are not suitable for intracortical or intraspinal stimulation because of insufficient charge injection capacity [7].

Intracortical stimulation requires using electrodes with very small areas, and therefore the researchers have developed faradic electrodes coatings based on three dimensional films of hydrate iridium oxide. "Iridium has electrochemical properties not shared by Pt or its alloys" [7]. These films can be formed by repeating the oxidation and reduction of the iridium on the metal surface, and this leads to greatly increase their ability to inject charge. Iridium oxide electrodes (IrOx) have a relatively large charge injection density and reversible faradic reactions [7].

Researches are now investigating the characteristics of TiN and IrOx using electrochemical techniques such as pulse stimulation, cyclic voltammetry (CV), and

electrochemical impedance spectroscopy (EIS). Pulse stimulation is a technique used to calculate the safe charge injection capacity of the electrodes. Usually fast varying current pulses are applied, whereby the safe charge injection capacity is the area under the voltage waveform before exceeding the water window. CV is a technique used to determine the operational water window limits, and to calculate the charge storage capacity of the electrode. It is used to study the capacitive and faradic behavior of the electrodes. EIS is a technique used to study the capacitive and faradic behavior of the electrodes as well by studying the Bode plot of the electrode. The next part will discuss what different groups have studied the characteristics of TiN and IrOx electrodes.

2.1.1 Weiland, Anderson, and Humayun Group

This group [5] "directly compared the electrical characteristics of iridium oxide and titanium nitride by fabricating silicon substrate probes that differed only in the material used to form the electrode". The silicon probes used in this work (provided by the University of Michigan) had five $4000\mu m^2$ octagonal electrodes. The sputtering technique was used to form both titanium nitride and iridium sites. They used three titanium nitride 5-site probes and two iridium oxide 5-site probes in which three electrodes on each material were studied in detail. In this work, both electrodes were characterized by the electrochemical techniques mentioned earlier. The next paragraphs will discuss the group work in more details.

A saturated calomel electrode (SCE) was used as a reference electrode, and a large platinum sheet as a counter electrode. All the measurements were made in a phosphate buffered saline. The CV measurements were obtained with 100mV/s triangle

wave from -600 mV to 700 mV. The impedance measurements were obtained with a 5mV sine-wave, 0.1-100kHz, -300, 0, 300 and 600 mV vs. SCE. Biphasic pulses of 25, 50, and 100 μA with duration of 100, 200, and 500μs were applied in the voltage measurements.

Figure 2.1 shows consistency in the electrical properties of the both the IrOx and TiN electrodes, that there is small standard deviation of the averaged impedance spectra. This figure also shows that the impedance amplitude of the TiN was 15% less than the iridium oxide at frequencies greater than 10kHz. The impedance amplitude of both materials is "nearly independent" of frequency at higher frequencies and becomes frequency dependent at lower values (below 4 kHz for TiN and below 0.5 kHz for IrOx). Since the frequency dependent impedance amplitude indicates capacitive charging as the dominant current flow process, "TiN becomes capacitive at a higher frequency than IrOx".

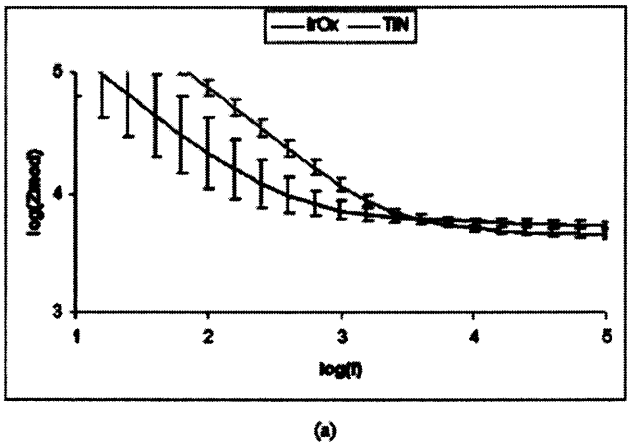

Figure 2.1 Impedance modulus. Measurement was taken with a 5-mV sine wave, dc potential 300 mV versus saturate calomel electrode. Averages of measurements from three electrodes of each type are shown. Error bars represent one standard deviation [5].

Figure 2.2 shows the cyclic voltammetry of TiN and IrOx. It is obvious from the figure that iridium oxide has a superior charge storage capacity, that the area under the IrOx CV is "significantly larger" than the area under the TiN CV. The IrOx CV had distinct peaks which implies reduction-oxidation reactions were involved. A reversibility of these reactions has been approved by other groups. The TiN CV had no distinct peaks, and thus an electrode current was dominated by capacitive current flow.

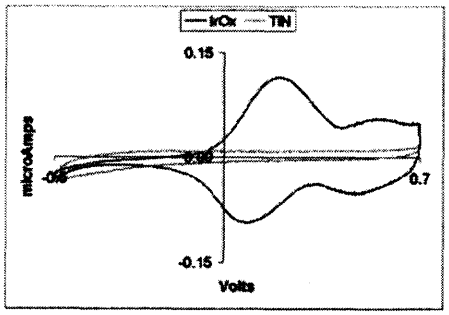

Figure 2.2 Cyclic voltammagrams of iridium oxide and titanium nitride electrodes [5].

Figure 2.3 shows the voltage measurements for TiN and IrOx in response to a current pulse. The iridium oxide generated a smaller voltage in all cases except when applying pulse duration less than 10μs (figure 2.3-a). By increasing the current pulse duration, the double layer charge would increase and lead to an increase in an electrode potential (figure 2.3-b, 2.3-c).

As mentioned, the charge injection limits is determined by determining the water window limits. It was found by applying 0.2ms anodic pulses that the safe charge injection for TiN is 0.87mC/ cm^2. The voltage limits were –0.6 to +0.8 V (water window minus the initial voltage drop). However, the safe charge injection for IrOx was measured to be 4mC/ cm^2 under the same conditions.

In summary, this group has studied the characteristics of both IrOx and TiN using electrochemical techniques such as pulse stimulation, CV, and EIS. This group has shown that iridium oxide has lower impedance and a higher charge storage capacity than titanium nitride, suggesting better performance as a stimulating electrode in applications that require high current densities.

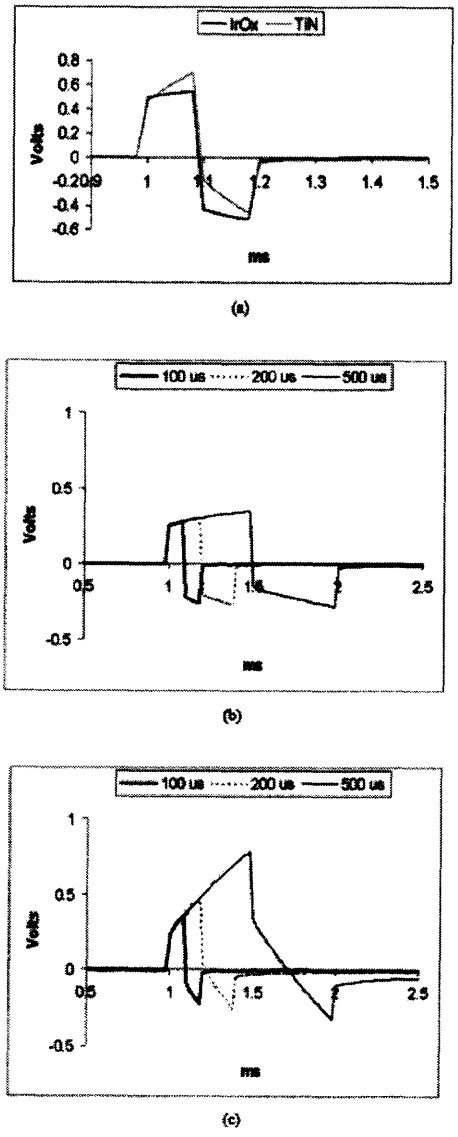

Figure 2.3 Voltage measured between current source and current sink in response to a current pulse. In all cases, current sink is a relatively large sheet of platinum. (a) Electrode potential for iridium oxide versus titanium nitride in response to a 100μA, 100μs current pulse. Electrode potential of (b) iridium oxide and (c) titanium nitride in response to 50μA pulses of varying duration [5].

2.1.2 Zhou and Greenberg Group

This group [4] has studied the University of Michigan electrodes (thin-film TiN coatings on Si substrate). The electrochemical techniques were used to characterize the electrodes. Figure 2.4 shows the 5 electrode microarray coated with thin-film TiN from University of Michigan.

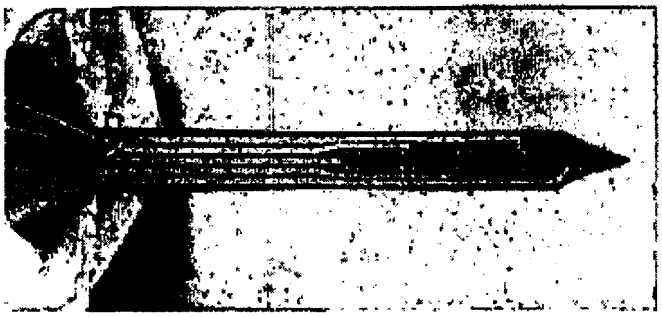

Figure 2.4 The 5 electrode microarray coated with thin-film TiN from University of Michigan [4].

This electrode has a diameter of 71.8μm and an area of $4.05 \times 10^{-5} cm^2$ and it has "multilayers of thin-film coatings including ~ 1μm TiN as the top layer of electrode material". This group determined the injectable charge using pulse stimulation (a cathodic first, biphasic charge-balanced current pulse with 1 ms pulse duration at 100 Hz.) in response to fast varying waveform as well as the electrode's stability. All tests were conducted at the room temperature using a large Pt electrode as a counter electrode and Ag/AgCl as a reference electrode. Phosphate buffered solution (PBS) and bicarbonate buffered solution (BBS) were used. EIS measurements were made at open circuit potential with a 10mV AC excitation potential, and at frequency from 100kHz to 1Hz.

This group has shown that TiN has no distinct peaks within the water window limits of –1V to 1.2V as shown in figure 2.5. This result is concordant with Weiland and Humayun group results. Figure 2.6 shows a typical Bode plot of a TiN electrode, the electrode impedance increases with decreasing the frequency indicating no faradic process was involved. The charge injection capacity measured for TiN is at 2.2 – 3.5mC/ cm^2 range (1ms pulse duration, with fast varying waveform). This value is considered "much higher than other capacitive electrodes such as Ta_2O_5".

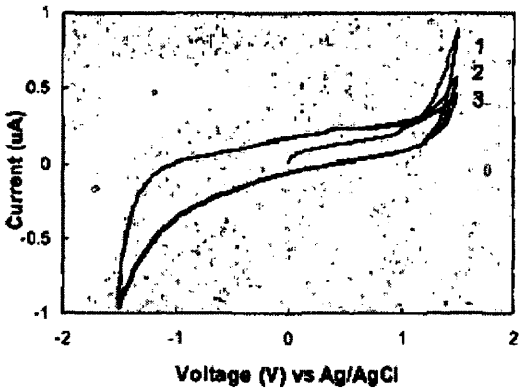

Figure 2.5 Cyclic voltammograms of a TIN electrode at a potential scan rate of 100mV/s [4].

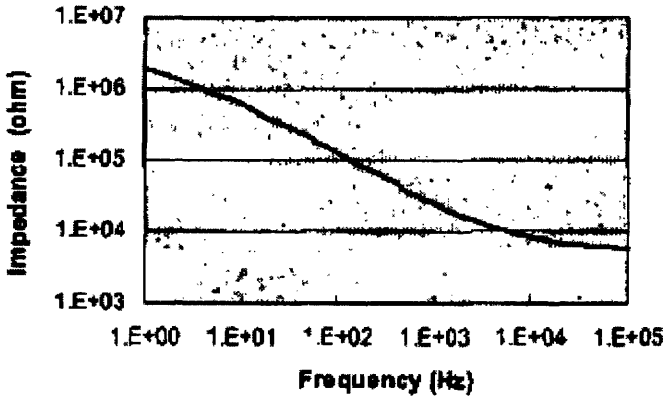

Figure 2.6 Bode plot of a TiN electrode measured at open circuit potential with an ac 10mV bias [4].

In summary, this group has studied the characteristics of TiN using electrochemical techniques such as pulse stimulation, CV, and EIS. This group has shown that there is no faradic process involved in titanium nitride electrode reactions. Furthermore, they measured the charge injection capacity of TiN and found it to be at 2.2–3.5 mC/ cm^2 range. This value is different than the value obtained by (Weiland, and Humayun) group which is 0.87mC/ cm^2. The discrepancy could be due to the difference (in materials) in the electrodes used in both studies.

2.1.3 Cogan, Plante, and Ehrlich Group

This group [8] has studied the activated iridium oxide films (AIROF) microelectrodes. They used potential biasing and biphasic, asymmetric current pulse waveforms to maximize the charge-injection capacity. These electrodes were fabricated at the Huntington Medical Research Institute, the exposed geometric surface area (GSA) of the iridium that used were either 1100 +- 100 μm^2 or 2000 +- 200 μm^2. "The exposed iridium was activated to AIROF by potentiodynamic pulsing between -0.6 and +0.85V versus Ag/AgCl in phosphate-buffered saline (PBS)".

The CV measurements were made at a sweep rate of 50mV/s between limits of 0.8 and -0.6V using Ag/AgCl as a reference electrode and a large area Pt as a counter-electrode in PBS. Potential transit measurements were conducted in carbonate and phosphate buffered saline solution (CBS/PBS). Bias levels from -0.1 to 0.7V were used, in which it is considered positive or negative with respect to the equilibrium open circuit potential of the AIROF (between 0.2-0.3V).

Figure 2.7 shows examples of asymmetric waveforms. Asymmetry defined as the

ratio of the cathodal to anodal pulse width, which introduced by "increasing the pulse width of the second pulse and decreasing the current accordingly to maintain charge-balanced".

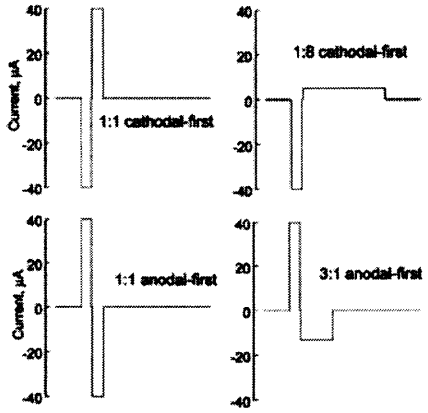

Figure 2.7 Examples of charge-balanced, biphasic current pulses (50 Hz, 0.4 ms leading phase) with different asymmetries in the cathodal and anodal pulse widths. The asymmetric cathodal-first 1:8 and anodal first 3:1 waveforms resulted in the highest charge injection capacities at positive and negative potential bias levels of 0.6 and 0.1 V, respectively [8].

Figure 2.8 shows the CV of an AIROF microelectrode with GSA equals to 1015μm^2 activated to a cathodic charge storage capacity (CSC_c) equals to 25mC/cm^2 (the hatched area). AIROF has distinct peaks at 0.1V and 0.2V. There are two strategies of asymmetries; cathodal-first current pulsing and anodal-first current pulsing. Figure 2.9 shows the charge injection limits of AIROF (cathodal first) as a function of anodic first and cathodal to anodal pulse width asymmetry (CSC_c = 29mC/cm^2). The open symbols show the 0.8V limit, and the closed ones show the -0.6V limit. It is obvious from the figure how the charge injection capacity increased using asymmetric pulses; the charge injection capacity with asymmetric pulses is 2.1 ± 0.9 times larger that that using symmetric pulses. Furthermore, the optimum results were at 0.6 V biases with 1:8 pulse

width ratios, that the mean charge injection capacity was $4.9 \pm 0.58 mC/cm^2$, compared with 0.3V bias ($3.1 \pm 0.4 mC/cm^2$).

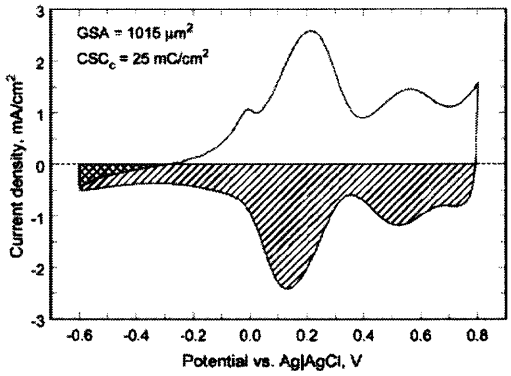

Figure 2.8 Cyclic voltammogram of an AIROF microelectrode [8].

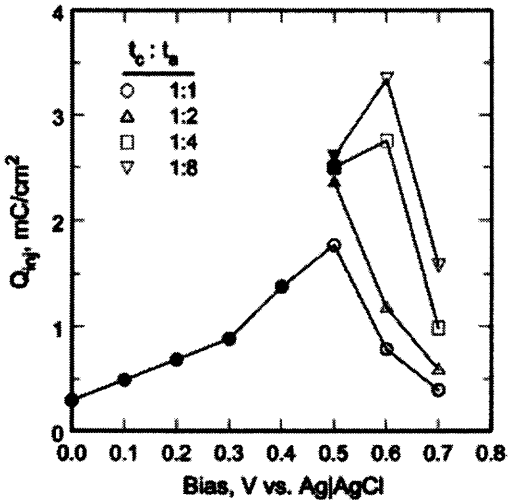

Figure 2.9 Charge-injection limits of AIROF (CSC = $29 mC/cm^2$, tip area $2024 \mu m^2$) subjected to biphasic, cathodal-first, current pulses as a function of bias potential and waveform asymmetry. The cathodal pulse width was 0.4ms. Closed and open symbols indicate whether the maximum negative or positive potential limit, respectively, limited the charge injection capacity [8].

The charge injection limits of AIROF (anodal first) as a function of bias and waveform asymmetry is shown in figure 2.10. In this strategy, they biased the AIROF to

a potential negative of its open circuit value. The maximum charge injection capacity with symmetric pulse was 4.2mC/cm^2 at a bias of 0.2V. However; the maximum charge injection capacity for 1:2 and 1:3 asymmetric pulses (anodal to cathodal) were 6.4mC/cm^2 and 9.6mC/cm^2 at 0.1V bias, respectively.

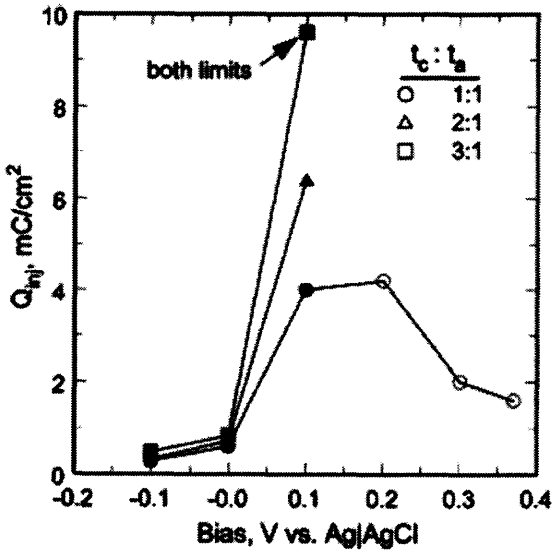

Figure 2.10 Charge-injection limits of AIROF (CSC = 25.1 mC/cm^2, tip area 2015 μm^2) subjected to biphasic, anodal-first, current pulses as a function of bias potential and waveform asymmetry. The anodal pulse width was 0.4 msec. Closed and open symbols indicate whether the maximum negative or positive potential limit, respectively, limited the charge injection capacity [8].

This group [9] has also introduced sputtered iridium oxide films (SIROFs) and compared them with the activated iridium oxide films (AIROFs). SIROF films were deposited by reactive sputtering from iridium metal in an oxidizing plasma. However, AIROF is formed from iridium metal by electrochemical potential cycling in an aqueous electrolyte. The characterization of sputtered iridium oxide films (SIROFs) as coatings for nerve electrodes is reported using the electrochemical techniques.

The cathodal charge storage capacity (CSCc) was calculated using slow sweep

rate CV measurements (50mV/s, phosphate buffered saline) between potential limits of –0.6V and 0.8 V, and this is an estimation for the total amount of iridium oxide deposited on the substrate. The EIS measurements were conducted using a 5mV rms sinusoidal excitation voltage about a fixed potential of 0.3 V vs. Ag|AgCl in CBS/PBS solution. All measurements were made using Ag/AgCl as a reference electrode and a large-area platinum as a counter electrode. The surface area of the electrodes was $0.05cm^2$.

The cyclic voltammetry measurements showed that both AIROF and SIROF (80nm thick) have cathodic charge storage capacity of $18mC/cm^2$. Figure 2.11 shows the cyclic voltammetry of both electrodes, it is obvious that SIROF does not have distinct peaks at 0.1V and 0.2V that are typical of AIROF. However, the charge is associated with faradaic reaction ($Ir^{3+} \Leftrightarrow Ir^{4+} + e^-$). SIROF exhibits slower redox reactions, which is "presumably due to the higher density of SIROF correspondingly lower ion transport rates within the films".

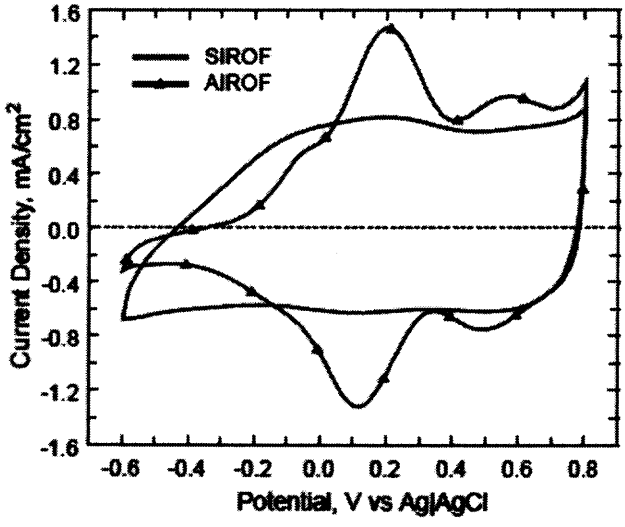

Figure 2.11 Cyclic voltammograms of SIROF and AIROF taken in PBS at a sweep rate of 50mV/s [9].

Bode plots measurements were made over a thickness range of 80-4600nm, with an uncoated Pt electrode included for comparison as shown in figure 2.12. SIROF showed the same behavior as the AIROF, below 1000 Hz the impedance decreases with increasing film thickness up to 2400nm.

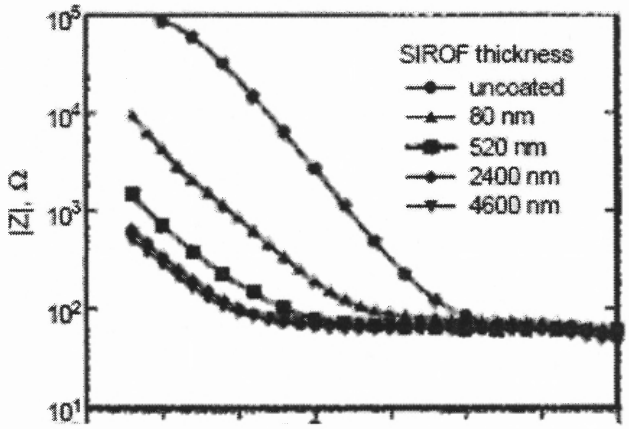

Figure 2.12 Impedance of SIROF in CBS/PBS as a function of film thickness [9].

Potential transit measurements are shown in figure 2.13 as a response of an 80nm thick SIROF. The charge injection capacity of SIROF was 0.37mC/cm^2 (before -0.6V limit) with 0.75ms monophasic cathodic pulses, which is "slightly higher" than that of uncoated Pt (~0.3). It was shown that the charge injection capacity increases with increasing the SIROF thickness, that the charge injection capacity of 580nm SIROF was 0.75 with a cathodal polarization of -0.32. SIROF can provide charge injection at levels beyond those of Platinum electrodes but still much less than AIROF.

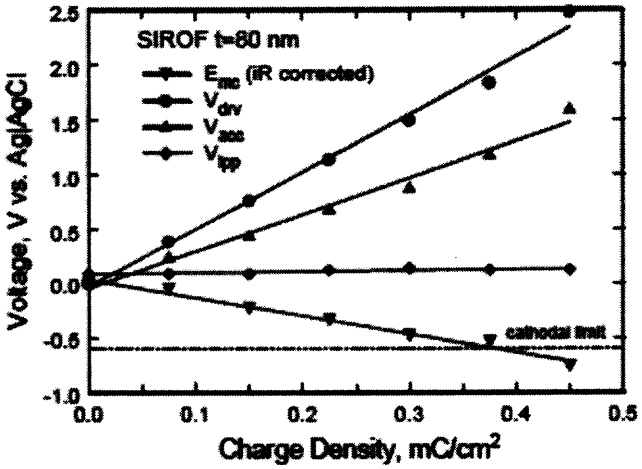

Figure 2.13 Potential transient response of an 80 nm thick SIROF in response to 0.75 ms cathodal current pulses [9].

Finally, this group [10] compared the charge injection limits of AIROF and Platinum-Iridium (PtIr) microelectrodes with similar geometric area and shape as shown in figure 2.14; they found that AIROF was capable of injecting between 4 and 10 times the charge of the PtIr.

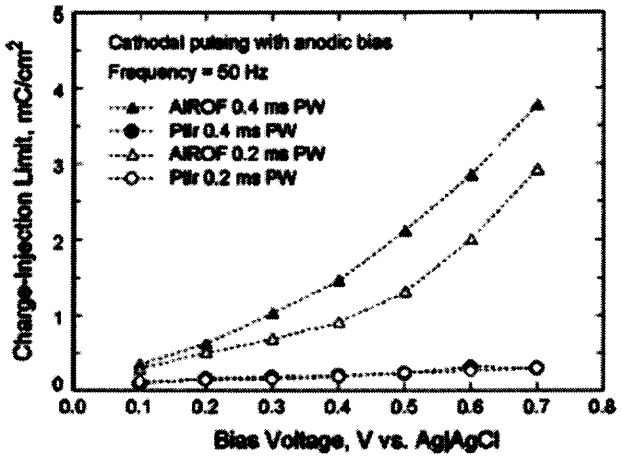

Figure 2.14 Comparison of the charge-injection limits of AIROF and PtIr as a function of bias and pulse width [10].

In summary, this group has investigated both AIROF and SIROF microelectrodes using the electrochemical techniques. "SIROF can provide charge-injection at levels beyond those of platinum electrodes (but much less than AIROF) and is more robust than AIROF" [9]. This may offer SIROF as an attractive alternative to other iridium oxides in some applications. This group has shown that the charge-injection capacity of AIROF is significantly increased by using either a positive bias for cathodal-first pulsing or a negative bias for anodal-first pulsing. Moreover, using asymmetric waveforms significantly increases the charge injection capacity with both cathodal-first and anodal-first current pulsing, in which the second phase is delivered at a lower current density and longer pulse duration.

2.2 Charge Injection Capacity Measurements:

This section will discuss our work in this field. As mentioned earlier, the size of the electrode plays a vital role in micro-level applications. The electrode contacts have to be small enough and generate sufficient charge for stimulation. TiN and IrOx have been investigated in this work as contact material. Various waveforms were introduced as alternative to the rectangular pulse to test the performance of these waveforms and to find out if more injectable charge can be obtained using the alternative waveforms comparing to the rectangular pulse. The charge injection capacity was obtained for TiN and IrOx electrodes. The charge injection capacity of TiN electrodes for an extended voltage range was also investigated.

2.2.1 Alternative Waveforms for TiN

Rectangular waveforms are commonly used as an input stimulus. In this study, we have introduced various waveforms as alternative input stimuli to the rectangular pulse. The charge injection capacity measurements were obtained for TiN electrodes in the water window limits. The behavior of the injected charge as a function of pulse width has been investigated.

2.2.1.1 Methods

The electrodes of TiN were provided by the Center of Neural Communication Technology at University of Michigan. The electrodes were placed in a phosphate buffered normal saline (ph=7.4) at room temperature. Large Ag/AgCl electrode was used as a reference. For measurements of charge injection capacity, rectangular, triangle, sinusoidal, exponential increase, exponential decrease, Gaussian, triangle decrease, and rectangular-last waveforms were used respectively. These waveforms were charge balanced, cathodic first, and biphasic current stimuli pulse train applied at 50Hz. The waveforms were applied using 20, 40, 60, 80, 100, 200, 300, and 500μs pulse widths. The current stimulator was custom designed to ensure a fast rise time (<0.5μs) and thereby allowing an accurate measurement of the access voltage at the onset of the current pulse.

The back voltage from the electrode was first buffered with a unity gain FET amplifier before sampled into a computer using data acquisition board (PCI 6071) and LabVIEW software (both from National Instruments) at a sampling rate of 1MHz. The bias voltage was set to 0V and the current amplitudes were determined that generated a

back voltage down to -1.2V. The initial voltage jump due to the access resistance was subtracted in calculation of the back voltage. Eight TiN contacts with an area of 177μm^2 were studied. Figure 2.15 shows the custom designed circuit used in this study.

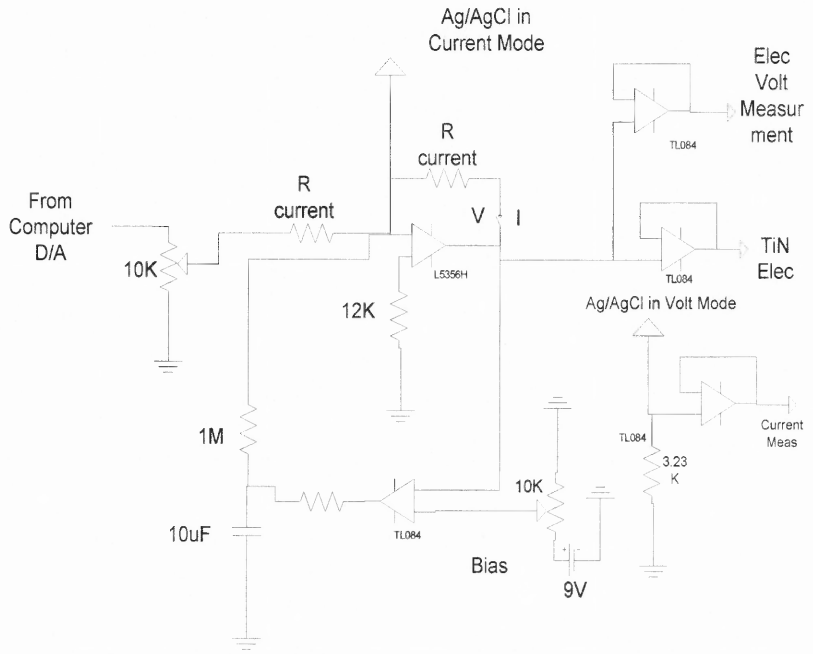

Figure 2.15 Custom designed circuit for charge injection capacity measurements.

2.2.1.2 Results and Discussion

Figure 2.16 shows the mean charge of the highest three TiN contacts using different waveforms as a function of pulse widths. Some contacts gave lower values comparing to the others. The highest three values were from the same contacts. It is obvious from the figure that the charge increases as the pulse width increase. The behavior of the all waveforms was the same (exponential increase with increasing the pulse width). Rectangle_last waveform gave the highest charge over the entire pulse width range whereas the Rectangle_first gave the lowest charge over the entire pulse width range. The

maximum charge obtained was 1.266mC/cm^2 using rectangular-last waveform at 500μs pulse width. The minimum charge at 500μs obtained was 0.536mC/cm^2 using rectangle-first waveform.

There is a significant difference applying the rectangle pulse first or last. The charge injection capacity has been changed while applying different waveforms between the two rectangular pulses. Triangle decrease waveform gave high charge over the entire pulse width range. Exponential increase waveform gave low charge over the entire pulse width range. There is a sudden increase in the charge after 300μs pulse width using the exponential decrease waveform that at 500μs pulse width the injected charge exceeded 1mC/cm^2.

Weiland group found the injected charge of TiN Michigan electrodes to be 0.87mC/cm^2 (0.2ms, -0.6 to 0.8V limit). At 0.2ms pulse width (-1.2V cathodic limit) we found it to be 0.96mC/cm^2. We obtained higher charge at 0.2ms because we clamped the voltage at -1.2V instead of -0.6. Zhou group found the injected charge at 1ms to be at 2.2-3.5mC/cm^2 range (-1-1.2V limit). At 0.5ms pulse width we found the injected charge to be 1.266mC/cm^2. Since the injected charge increases with increasing the pulse width, higher charge at 1ms pulse width is expected.

In conclusion, different kinds of waveforms can be used as alternative to the rectangular waveform such as triangle decrease waveform. Triangle decrease wave form gave charge close to the rectangle_last waveform over the entire pulse width range. The rectangle pulse is superior over the other waveforms since it gave the highest charge over the entire pulse width range. The Injected charge of TiN electrodes is much higher than other capacitive electrodes such as Ta_2O_5 with injected charge at a range of 0.016-

0.12mC/cm^2 [4] and Pt and Ptlr-alloys electrodes at a range of 0.05-0.15mC/cm^2 [7]. This range of TiN electrodes injectable charge (0.3-1.27mC/cm^2, rectangular pulse-last) is useful for different kind of microstimulation applications as shown in Table 2.1.

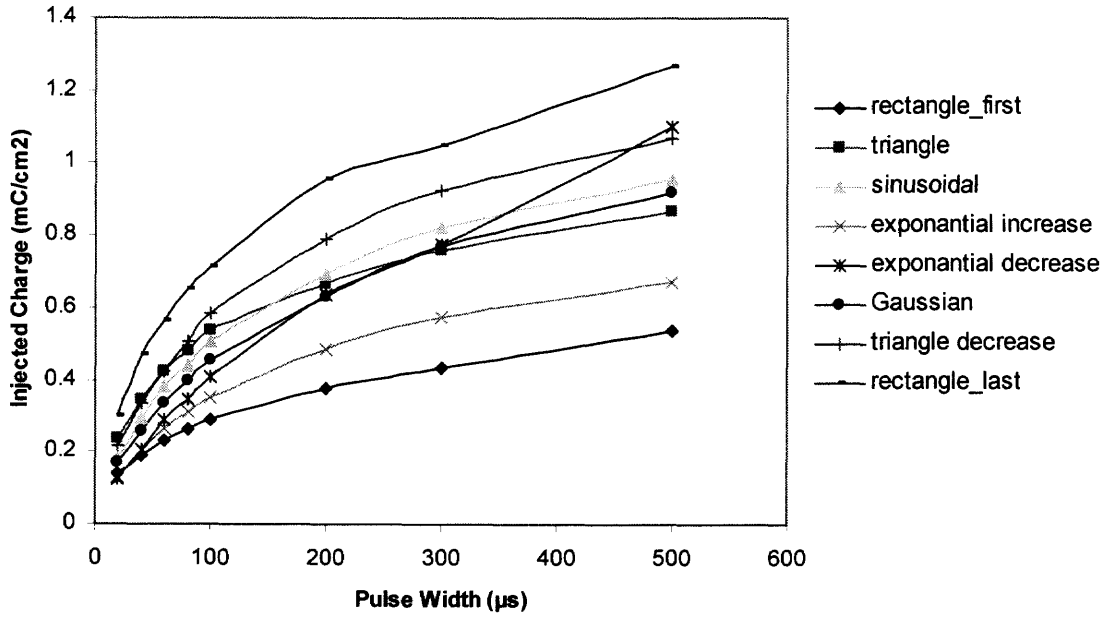

Figure 2.16 Alternative waveforms for TiN. The charge injection capacity is plotted as a function of pulse width.

2.2.2 Alternative Waveforms for IrOx

Also alternative waveforms were used with IrOx electrodes. As mentioned, IrOx has been introduced as an electrode material for micro-stimulation applications. The behavior of the IrOx electrode with different pulse widths also has been investigated. The charge injection capacity was obtained in the water window limit.

2.2.2.1 Methods

Also the IrOx electrodes were provided from the University of Michigan. The same method was used with IrOx. Rectangular, exponential increase, exponential decrease, linear decrease, sinusoidal, Gaussian, and linear increase waveforms were used. The bias voltage was controlled with the custom-built circuit shown in figure 2.15. The bias voltage was set to 200 mV and the current amplitudes were determined that generated a back voltage down to -0.6V. Three IrOx contacts with an area of 177μm^2 were studied.

2.2.2.2 Results and Discussion

Figure 2.17 shows the mean charge for three IrOx contacts using different waveforms as a function of pulse widths. Some contacts gave lower values comparing to the others. It can be concluded from the figure that the charge exponentially increases with increasing pulse width and this is consistent with TiN electrodes measurements. Linear decrease waveform gave the highest charge over the entire pulse width range. Exponential increase gave the lowest charge over the entire pulse width range. The maximum charge obtained was 0.98mC/cm^2 using linear decrease waveform at 500μs pulse width. The minimum charge at 500μs obtained was 0.45mC/cm^2 using exponential increase waveform. The exponential increase waveform gave low value. The sinusoidal, rectangle and Gaussian waveforms generated high values of charge (comparing to the other waveforms) over the entire pulse width range.

The measured charge injection capacity of IrOx obtained in our laboratory (0.98mC/cm^2, 0.5ms, -0.6V cathodic limit) is much smaller than the one measured by Weiland group (4mC/cm^2, 0.2ms, -0.6 to 0.8V limit). In our work, we used only three

contacts and these contacts could have been partially damaged after applying many waveforms. Although the injected charge of IrOx was low, we still can compare the charge injection capacity using different waveforms and test the performance of each waveform. In conclusion, linear decrease waveform gave higher charge than the rectangular waveform which warrants further investigation of the linear decrease waveform.

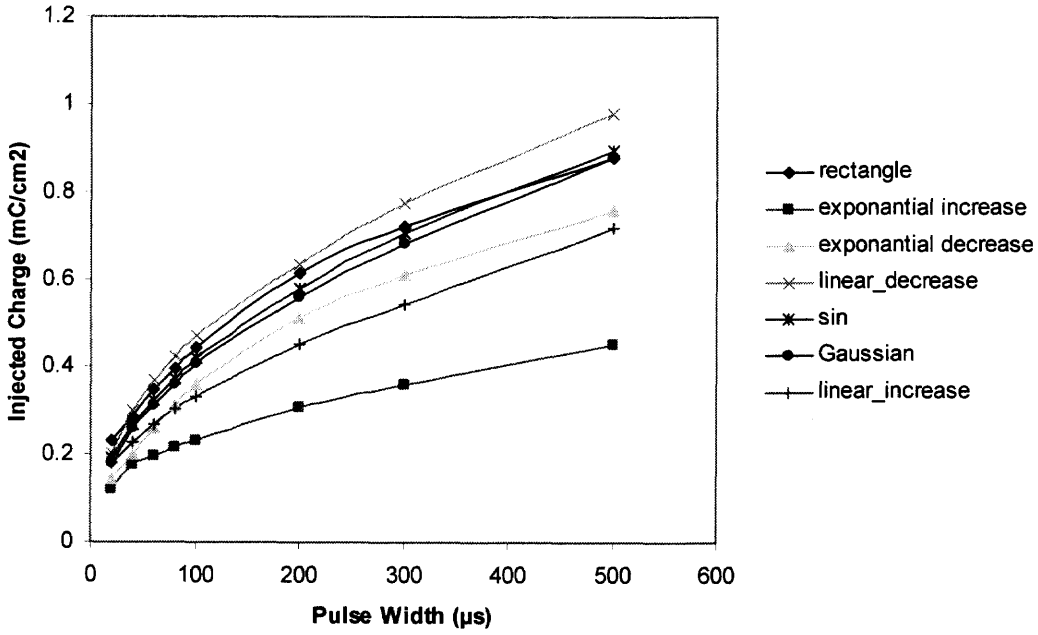

Figure 2.17 Alternative waveforms for IrOx. The charge injection capacity is plotted as a function of pulse width.

2.2.3 Charge Injection Capacity of TiN Electrodes for an Extended Voltage Range

The water window limit is the operational limit for an electrode, several groups reported on maximum injectable charge of TiN electrodes within the water window limit (-1.2V, slow cyclic voltammetry, 5mV/s). However, another group has tested rough surface TiN electrodes using voltammetry at fast sweeping rates (>10V/s) within the voltage range of

-3.0V to 1.0V. As a results, neither oxidation/reduction nor hydrogen adsorption/desorption peaks could be observed. This group claimed that the charge-transfer process was "almost completely reversible" for this voltage range and no evidence of bubble generation was seen. In this work, we investigated the maximum injectable and the recoverable charges with TiN electrodes for extended cathodic voltages using current and voltage pulsing.

2.2.3.1 Methods

The electrodes of this study were the University of Michigan electrodes. The electrodes were placed in a phosphate buffered normal saline (ph=7.4) at room temperature and the bias voltage was controlled with the custom-built circuit (figure 2.15) with respect to a large Ag/AgCl reference electrode. For measurements of charge injection capacity, a charge balanced, cathodic first, biphasic current stimulus pulse train was applied at 50Hz. Both cathodic and anodic phases were 0.5ms long and of the same amplitude. The current stimulator was custom designed to ensure a fast rise time (<0.5μs) and thereby allowing an accurate measurement of the access voltage at the onset of the current pulse. The back voltage from the electrode was first buffered with a unity gain FET amplifier before sampled into a computer using data acquisition board (PCI 6071) and LabVIEW software (both from National Instruments) at a sampling rate of 1MHz. Spike triggered averaging method was employed to reduce the noise signal. The bias voltage was set to -0.8, -1.0, and -1.2V and the current amplitudes were determined that generated a back voltage down to -3.0V in steps of -0.2V. The initial voltage jump due to the access resistance was subtracted in calculation of the back voltage. Six TiN contacts with an area of 177μm^2

were studied.

For the measurements of the recoverable/unrecoverable charge, six TiN contacts with larger surface areas (4000μm^2) were used to minimize the measurement errors of electrode current. A single cathodic voltage pulse (0.5ms) with varying amplitude (0 to -3.0V) was applied. The voltage was clamped at zero following the pulse. The electrode current was integrated during the cathodic phase to find the injected charge and during the following 50ms as the charge recovered from the electrode. The difference of the two was taken as the unrecoverable charge.

2.2.3.2 Results and Discussion

Figure 2.18 shows the back voltage with one of the contacts as a response to current pulse of 18μA (thick line) and 16μA (thin line). The current amplitude was increased until the H2 evolution was evident with a plateau at the end of the cathodic cycle. The pulse duration was 0.5ms, and the bias voltage was -1V. The first plateau (thick line) shows a distortion at the end of the cathodic phase around -3.5V suggests faradaic reactions occur. However, the second plateau (thin line) shows no distortion. The voltage step due to the access resistance was about -0.2V within the first 2μs.

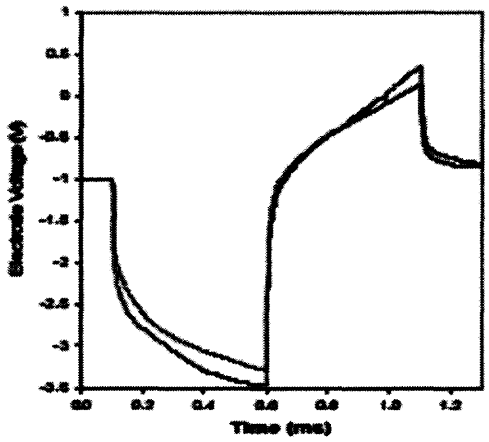

Figure 2.18 The electrode voltage with one of the contacts for a bias potential of -1.0V.

Figure 2.19 shows the mean charge for six TiN contacts as a function of electrode voltage during a cathodic current pulse with a 0.5ms duration for three different bias voltages; -0.8, -1.0, and - 1.2V. The maximum injectable charge was 4.45mC/cm^2 at the peak electrode voltage of -3.0V. This value is higher than 2.2-3.5mC/cm^2 [4] and 0.9mC/cm^2 [5] reported earlier for the same pulse width. For most of our measurements, the distortion occurred in the anodic phase when the holding potential was made more positive than -0.9V. The maximum values of the total injectable charge with minimum distortion were obtained for the bias voltages more negative than -1.0V (as shown in figure 2.19). There was no evidence of bubble generation under microscopic observation with high magnification (x130).

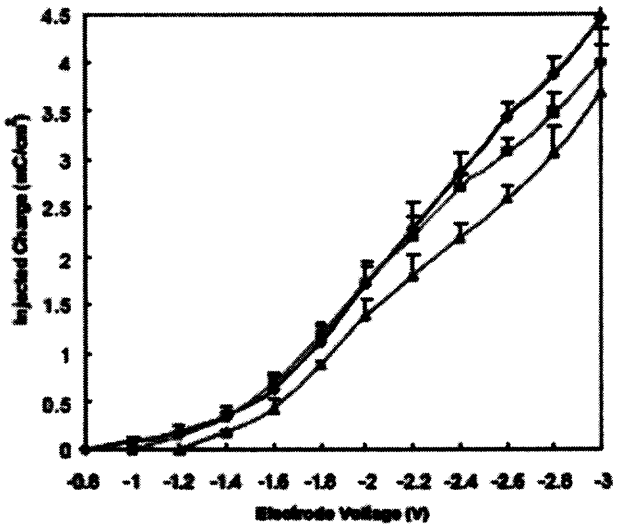

Figure 2.19 Injected charge as a function of electrode voltage during a cathodic current pulse with a 0.5ms duration for three different bias voltages; -0.8 (blue), -1.0 (pink), and -1.2V (red). The mean charge for six TiN contacts and the standard deviations are shown (vertical bars).

Figure 2.20 shows the unrecoverable charge plotted as a percentage of total injected charge against the voltage pulse amplitude. Within the water window, the unrecoverable charge was a little over 1%. The unrecoverable charge for the extended voltage limits remained under 7% of the total injected charge. This small increase cannot account for such a large change in the charge injection capacity. Most of this increase must be provided by fast recoverable faradaic reactions.

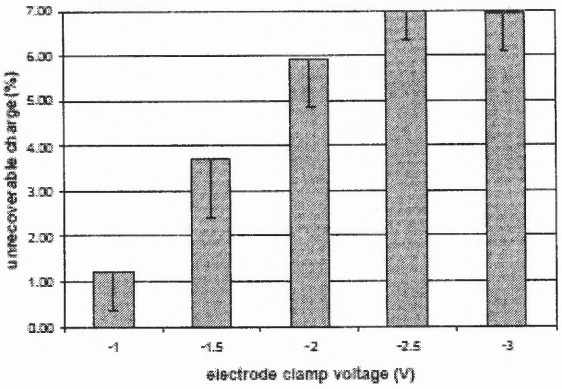

Figure 2.20 Unrecoverable charge as a percentage of the total injected charge for voltage pulse amplitudes varying from -1V to -3V. The pulse width is 0.5ms and the electrode. surface area is 4000μm^2. Standard deviations are vertical bars (n=6).

The large values of charge injection capacity of TiN and relatively small unrecoverable charges warrant further investigation of the charge injection mechanism and the feasibility of safe neural stimulation in TiN interfaces at extended range of electrode voltages.

2.2.4 Conclusion

It can be concluded from the TiN and IrOx electrodes results that the injected charge is high when the amplitude of the current stimulus decreases as a function of time. On the other hand, the injected charge is low when the amplitude of the current stimulus increases as a function of time. Both IrOx and TiN allow sufficient charge injection for FLAMES approach. TiN is preferred for future experimentation since TiN does not require a bias voltage to achieve useful charge injection rates, and thus is a good choice as an electrode material in this application.

CHAPTER 3

OPTICAL PROPERTIES OF RAT NEURAL TISSUES

3.1 Introduction

Near-infrared light (NIR), ranging from 700 to 900 nm, has the maximum penetration depth in white and gray matters of the nervous system [12]. This property has been utilized in numerous applications ranging from spectroscopic imaging [13] to treatment of brain tumors [14]. In these applications, knowledge of optical properties of the human neural tissue is crucial to determine the specific wavelength range where light penetration depth is maximum [15]. However, it is equally important to know the optical properties in the animal models for development of such applications. The rat nervous system has been frequently used as an animal model in testing of these devices [16]. In our laboratory, we are also interested in transferring energy to an implantable microstimulator (FLAMES) by optical means in the NIR wavelengths [17]. There are numerous reports on optical properties of human neural tissue [15], [20], [21]. But, the literature from the experimental animals is very limited and the reported values are varying substantially.

In our study, the microstimulator is implanted inside the neural tissue, and therefore light must penetrate a few millimeters through the tissue before reaching the device. As the light travels into the tissue, its intensity decreases due to absorption and scattering. Some of the incident light also reflects back at the surface of entry. The decaying of the light energy inside the tissue is governed by Beer's law (figure 3.1). One way of expressing Beer's law is

$$It = Io \times (1 - R) \times e^{\frac{-x}{a}} \qquad \text{(Equ. 3.1)}$$

where *It* is the transmitted and *Io* is the incident light energy. *R* is the reflection coefficient of the surface and *a* is the penetration depth. Penetration depth is defined as the distance at which the total optical power is reduced to 37% of the incident light. For direct measurements of light absorbed or scattered, the tissue should be very thin (thickness << 1/scattering coefficient) [24].

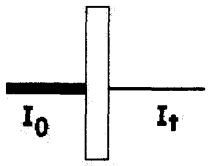

Figure 3.1 Diagram of Beer absorption of a beam of light as it travels through a material of known thickness.

There are three main types of spectroscopy; (1) **Absorption spectroscopy**: it is a device that measures the radiation absorbed by a sample as it is excited to higher energy levels. (2) **Emission spectroscopy**: it is a device that relies upon exciting a sample and then measuring the radiation emitted as the sample falls down to lower energy levels. (3) **Scattering spectroscopy**: it is a device that measures certain physical properties by measuring the amount of light that a substance scatters at certain wavelengths, incident angles, and polarization angles. Moreover, NIR specroscopy is well known for medical applications. **NIR specroscopy** "is a spectroscopic method utilising the near infra-red region of the electromagnetic spectrum (from about 800 nm to 2500 nm)" [18].

NIR spectroscopy has differnet kind of biomedical applications using the wave length of 700 to 900 nm, "where light scattering is more prominent than light absorption"

[19]. There are diffrences between healthy and disease tissues in light scattering properties due to the possible changes in cellular and intracellular structures. One of these applications is to detect both physiological and pathological conditions of tissues, including blood flow and hemoglobin concentration measurements, also including cancer diagnosis and tissue distinction [19].

In brain applications, an optical diffuse tomography (type of monitoring and imaging modality) is used. In this technique there is a possibility to obtain physiologically relevant information about the oxygen saturation of brain tissue. However, quantitative information can not be retrieved unless the optical properties of the brain tissues are known. Laser-induced interstitial heating of deep brain tumors is promising minimally invasive therapeutic procedures for the treatment of neoplastic lesions. The optical properties of tumors and of surrounding native brain tissue are needed to obtain successful therapy planning. For optimal laser thermotherapy treatment, knowledge of brain optical properties is required to determine the specific wavelength range where light penetration depth is maximum [15].

The main purpose of this chapter is to measure the transmitted light power through the rat neural tissues to measure how deep the FLAMES can be implanted into the peripheral and central nervous system and still be activated. In this chapter, we report the transmittance, penetration depth, and reflectance for NIR light in the rat neural tissues including the sciatic nerve, and the brain cortex.

In the next part, I will talk about various groups that have studied the optical properties of different types of human and animal tissues. In our project, we are using the same principles and techniques that are used in NIR spectroscopy.

3.1.1 Yaroslavsky, Schulze, and Schober Group

This group [15] has investigated the optical properties of native and coagulated human brain tissues *in vitro* in the visible and near infrared spectral range. White brain matter, grey brain matter, cerebellum and brainstem tissues were investigated in this work. In addition, two human tumors were investigated. All samples were stored at low temperature (2-3 °C, < 48h). The white matter samples had a thickness of 80-200μm. All other samples had a thickness of 100-200μm. An integrating-sphere technique was used to measure the diffuse reflectance, total transmittance, and collimated transmittance of the samples. By using inverse Monte Carlo technique, the absorption coefficients, the scattering coefficients and the anisotropy factors of the samples were determined from the experimental data. Moreover, the values of reduced scattering coefficient and light penetration depth were evaluated. For the purpose of this study, the results of the brain white and grey matter only will be discussed.

The results of the optical properties of white and grey brain matters are summarized in figures 3.2 and 3.3. Both white and grey brain matter had similar dependencies of the optical properties on the wavelength. "The scattering coefficients decreased and the anisotropy factor increased with the wavelength". The absorption behavior of all tissues resembled a mixture of oxy- and deoxy- hemoglobin absorption spectra. The reason it was "not possible to remove all blood residuals from the sections". White brain matter had "substantially higher" extinction coefficients than those of grey brain matter over the entire spectral range. Light penetration depth of grey matter was greater than that of white matter.

The values of absorption and scattering coefficients increased for both white and

grey matter after coagulation. Histological analysis has shown that coagulation causes brain tissue shrinkage and condensation, and therefore concentration of chromophores and scattering inhomogeneities increases and tissues become optically denser. As a result, both scattering and absorption coefficients increase significantly in the spectral range. The anisotropy factors of white brain matter and grey brain matter "remained nearly unchanged".

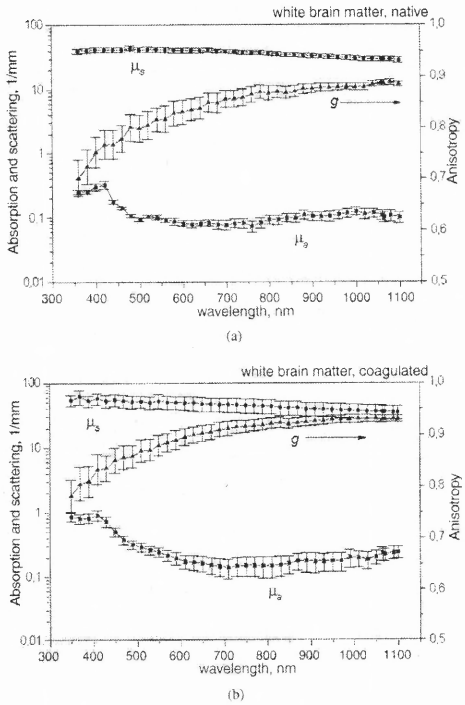

Figure 3.2 Optical properties of human white brain matter. Average of seven samples. Squares: absorption coefficient, circles: scattering coefficient, anisotropy factors and bars: standard errors. (a) Native samples and (b) coagulated samples [15].

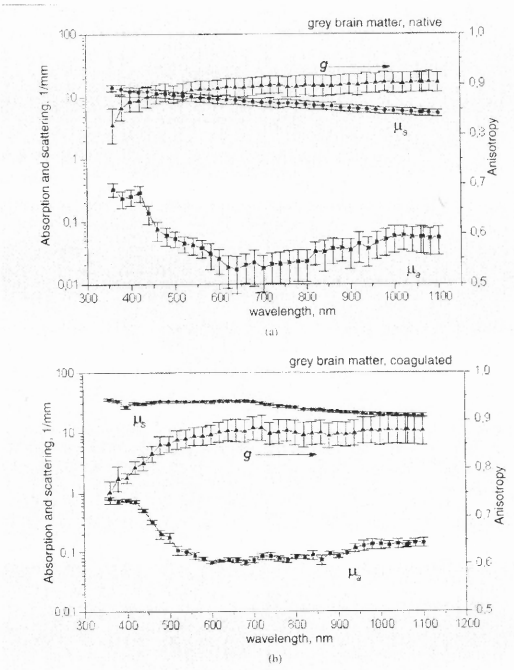

Figure 3.3 Optical properties of human grey brain matter. Average of seven samples. Squares: absorption coefficient, circles: scattering coefficient, anisotropy factors and bars: standard errors. (a) Native samples and (b) coagulated samples [15].

Table 3.1 and 3.2 show the optical properties of white and grey brain matters published in the literature compared to those obtained in this work. It can be concluded from table 3.1 that light penetration depth of white brain matter is "substantially lower" than that of grey matter. On the other hand, there are differences in absorption and scattering coefficients. This discrepancy may be explained by the different theoretical approaches used in different studies, and the different sample preparation techniques. It can be concluded from the tables that light penetration depth is "substantially reduced" after coagulation (Table 3.2).

Table 3.1 Optical Properties of Native Human Brain Tissues

Biotissue	λ (nm)	μ_a (mm^{-1})	μ_s (mm^{-1})	g	μ_s' (mm^{-1})	δ_{eff} (mm)	Reference
White brain matter	456	0.81	92.3	0.92	7.384	0.22	Gottschalk (1992)
	450	0.14	42.0	0.78	9.24	0.5	*
	514	0.5	104.5	0.93	7.315	0.29	Gottschalk (1992)
	510	0.1	42.6	0.81	8.094	0.64	*
	630	0.15	38.6	0.86	5.404	0.63	Gottschalk (1992)
	630	0.08	40.9	0.84	6.544	0.79	*
	675	0.07	43.6	0.87	5.668	0.83	Gottschalk (1992)
	670	0.07	40.1	0.85	6.015	0.83	*
	850	0.08	14	0.95	0.7	2.3	Roggan *et al* (1994)
	850	0.1	34.2	0.88	4.1	0.9	*
	1064	0.16	51.3	0.95	2.565	0.88	Gottschalk (1992)
	1064	0.04	11	0.95	0.55	3.76	Roggan *et al* (1994)
	1064	0.1	29.6	0.89	3.256	1.0	*
Grey brain matter	456	0.9	68.6	0.95	3.43	0.29	Gottschalk (1992)
	450	0.07	11.7	0.88	1.404	1.84	*
	514	1.17	57.8	0.97	1.734	0.31	Gottschalk (1992)
	510	0.04	10.6	0.88	1.272	2.52	*
	630	0.14	47.3	0.93	3.311	0.83	Gottschalk (1992)
	630	0.02	9.0	0.89	0.99	4.06	*
	675	0.06	36.4	0.91	3.276	1.29	Gottschalk (1992)
	670	0.02	8.4	0.9	0.84	4.4	*
	1064	0.19	26.7	0.96	1.07	1.18	Gottschalk (1992)
	1064	0.05	5.7	0.9	0.57	3.28	*

Note: Obtained in Yaroslavsky (*) and Known From the Literature. Wavelength (λ (nm)), Absorption Coefficient (μ_a (mm^{-1})), Scattering Coefficient (μ_s (mm^{-1})), Anisotropy factor (g), reduced scattering Coefficient (μ_s (mm^{-1})), and Light penetration depth (ζ (mm)) [15].

Table 3.2 Optical Properties of Coagulated Human Brain Tissues

Biotissue	λ (nm)	μ_a (mm^{-1})	μ_s (mm^{-1})	g	μ_s' (mm^{-1})	δ_{eff} (mm)	Reference
White brain matter	850	0.09	17	0.94	1.02	1.83	Roggan *et al* (1994)
	850	0.09	30	0.88	3.6	1.01	*
	1064	0.05	13	0.93	0.91	2.6	Roggan *et al* (1994)
	1064	0.1	27	0.89	2.97	1.06	*

Note: Obtained in Yaroslavsky (*) and Known From the Literature [15].

In summary, the results obtained from this work are in qualitative concordant with the literature. However, differences exist and "most probably" due to the various

theoretical models and sample preparation techniques employed. The spectral range of 1000-1100nm is the optimal wavelength range for therapeutic and diagnostic light applications, where the light penetration depth is maximal. The optical properties changed "dramatically" after coagulation. This is an important factor which should be carefully considered in treatment planning.

3.1.2 Eggert and Blazek Group

This group [20] has investigated the optical properties between 200 and 900nm of meninges, normal human brain tissue, and brain tumors. According to Beer's law, penetration depth was calculated from reflection and transmission measurements. The relative levels of absorption and scattering were evaluated according to Kubelka-Munk theory from the relative level of reflection measured in tissues samples more than 5mm thick.

A two-beam spectral photometer with an integrating sphere was used as a measuring instrument. The materials contained 13 brains and 1 specimen each of dura matter, flax, and arachnoid obtained at autopsy and 30 samples of brain tumors (17 meningiomas, 5 glioblastomas, and 8 low grade gliomas) removed during operation. The investigated samples were frozen by immersion in liquid nitrogen and stored at -18°C. The slice thicknesses were 0.32, 0.55, and 0.62mm. The penetration depth was calculated from reflectance (R) and transmittance (T) measurements with regard to the sample thickness (d) used as follow:

$$a = \frac{-d}{\ln(\frac{T}{100-R})} \qquad \text{(Equ. 3.2)}$$

For the purpose of this study, the results of the brain white and grey matter only will be discussed. Both grey and white brain matter shared common features. Reflectance increased with the wavelength within the visible spectral range, and remind unchanged between 600 and 900nm. The penetration depth increased with increasing the wavelength. The absorption bands of hemoglobin interrupted the increase in both penetration depth and reflectance. Absorption decreased with the wavelength. On the other hand, scattering "slightly" increased within (200-600nm) spectral range, and showed "nearly no changes" within the red and near infrared spectral range of the grey matter. "Surprisingly, scattering decreased considerably in white matter beyond 600nm". The back scattering fraction of the incident optical power is included within the measured reflectance.

Figure 3.4 and 3.5 show the relative levels of reflection (R), absorption (K), and scattering (S) as a function of wavelength for gray and white matter respectively. Reflection of white matter is "considerably" higher and absorption is lower than in gray matter. In the red and near infrared spectral range of the white matter, most of the incident optical power was reflected and only minimal absorption was found. As mentioned, scattering remained constant in grey matter but decreased considerably in white matter beyond 600nm. In the range from 300 to 900nm, there were significant differences between grey and white matter regarding reflection, absorption, and scattering. Samples containing considerable amount of gray matter besides white matter

were investigated. It was found that "nearly" the same optical properties obtained as in pure grey matter (as shown in figure 3.6). Figure 3.7 shows the penetration depth of gray and white matter. Gray matter penetration depth was "nearly twice" that of white matter (high statistical dispersion between 600 and 900nm).

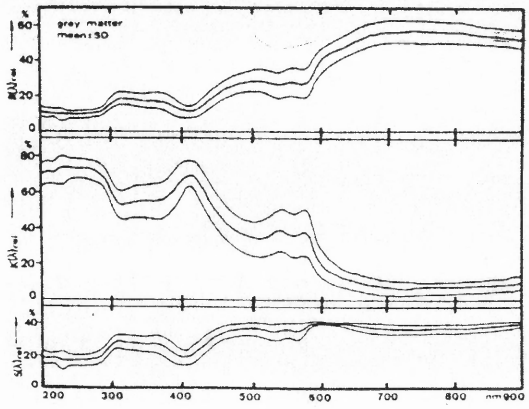

Figure 3.4 Frontal grey matter (n=13): relative levels of reflection (R), absorption (K), and scattering (S) plotted against wavelength [20].

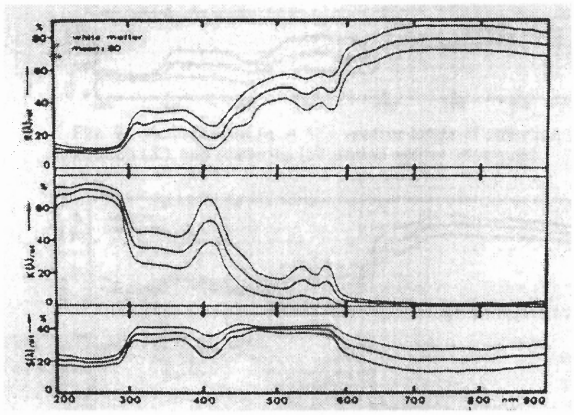

Figure 3.5 Frontal white matter (n=13): relative levels of reflection (R), absorption (K), and scattering (S) plotted against wavelength [20].

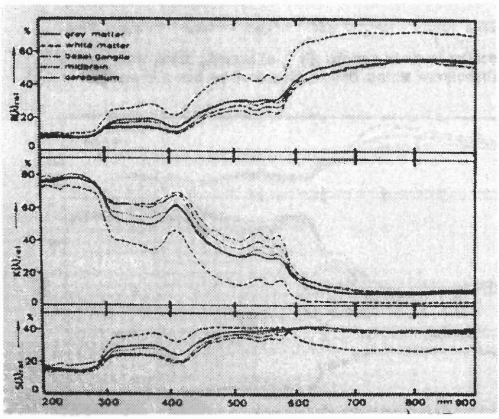

Figure 3.6 Frontal grey matter, frontal white matter, basal ganglia, midbrain, and cerebellar hemisphere (one sample of each): relative levels of reflection (R), absorption (K), and scattering (S) plotted against wavelength [20].

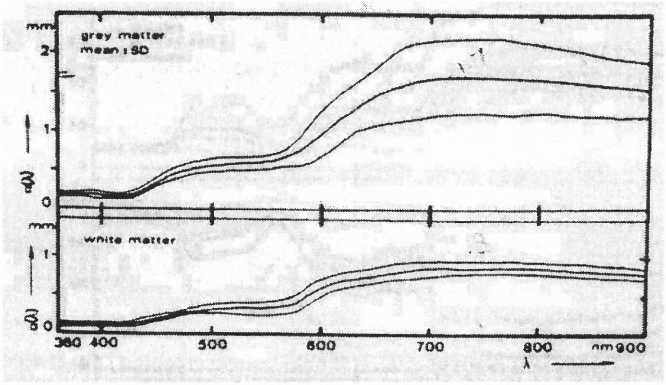

Figure 3.7 Frontal grey (n=13) and white (n=13) matter: penetration depth (a) plotted against wavelength [20].

Finally, I would like to compare the previous two group's results. Both groups showed the dependency of the optical properties to wavelength. The first group (Yaroslavsky, Schulze, and Schober) showed that the scattering coefficient slightly decreased within the investigated wavelength (300-1100nm) in white and grey brain matter; however the second group (Eggert and Blazek) showed that the scattering (fraction from the incident optical power) slightly increased within 200-600nm

wavelength in grey and white brain matter. Beyond 600nm, scattering remained constant in grey matter but decreased considerably in white matter. Regarding to the absorption measurements, the first group was not able to measure it accurately because of the difficulty in removing all blood residuals from the sections. The second group showed that the absorption is higher in gray matter than in white matter (remnants of blood were removed without any mentioned difficulties). Both groups showed that the gray matter penetration depth is higher than that of white matter, but with quantitative discrepancies. Within the near infrared range, the first group evaluated the penetration depth to be 0.9-1.0mm in white matter and 3.28mm in grey matter (table 3.1). The second group evaluated the penetration depth to be 0.75mm in white matter and 1.5mm in grey matter (figure 3.7).

There are similarities as well as discrepancies between the two groups. The discrepancies are due to the fact that (1) each group used different theoretical approach; the first group used inverse Monte Carlo technique and the second group used Kubelka-Munk theory, (2) each group used different measurement technique, and (3) sample preparation method was different between the two groups.

3.1.3 Svaasand and Ellingsen Group

This group [21] has investigated the optical properties of the human brain in the wavelength region from blue to near infrared; penetration depth of neonatal and adult brain was calculated. The measurements were conducted on five human brains immediately after autopsies which were carried out 1-2 days post mortem.

Optical fiber was used to couple the light into the center of the tissue samples.

The fiber had a core diameter of 200μm and nominal numerical aperture of 0.2. The optical loss of the fiber was less than 30dB/km for all wavelengths from 488nm to 1060nm. The detected light was measured using silicon PIN detector.

Figure 3.8 shows the results for penetration depth in the red part of the spectrum. This figure shows that the penetration depths for the adult brains are systemically smaller than the corresponding value for the neonatal brain. Furthermore, the penetration depth in the grey matter was slightly larger than in the white matter. But according to this group the differences were less than 10% for all wavelengths. The results for penetration depth for various colors are summarized in Table 3.3. It is obvious from the table that the penetration depths increase with increasing the wavelength.

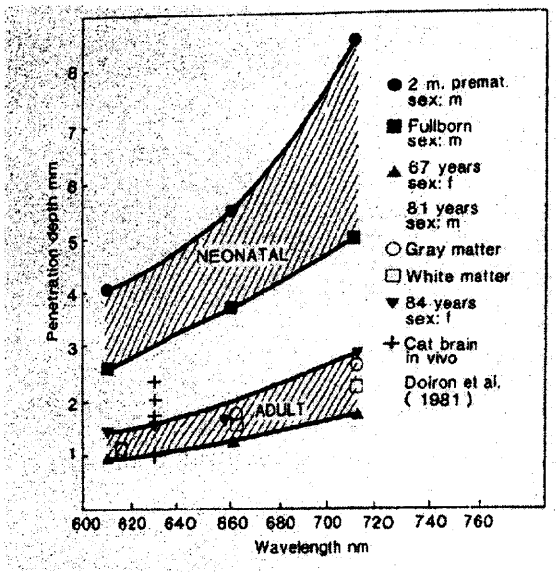

Figure 3.8 Optical penetration depth for red light in human brain tissue [21].

In summary, this group has shown that the corresponding values for the penetration depth in the neonatal brain are "typically 2-3 times larger" than that in the fully myelinated adult brain at all wavelengths. "The results indicate that the penetration

depth in adult brain tissue is dominated by the joint action of hemoglobin absorption and scattering from myelin. Thus, the penetration is strongly dependent on the degree of myelination".

Table 3.3 Optical Penetration Depth of Human Brain Tissue

Color	Wavelength (nm)	Age: 2 months premature Sex: M	Age: full-born Sex: M	Age: 67 years old Sex: F	Age 81 years old, Sex: M		Age: 84 years old Sex: F
					Gray matter	White matter	
Blue	488	1.7	1.3	0.4	0.5	0.5	0.7
Green	514	1.7	1.1	0.4	—	—	0.6
Red	660	5.4	3.7	1.2	1.7	1.6	1.6
Near-infrared	1060	8.8	7.1	3.2	3.5	2.9	4.3

Penetration depth in mm measured 1–2 days post mortem.

Note: Ref [21].

Before talking about our work in this field; the optical properties of rat neural tissues, the transmitted light power measurements, and penetration depth/reflectance calculations I will talk about the laser source and the calibration procedures for it.

3.2 Laser Calibration:

A NIR laser source (DLS-500-830FS-100, StockerYale, Canada) is used in this work. This source has an 827.3nm wavelength, and 73.8mW power. The NIR source is controlled via a voltage control circuit built inside and this circuit is controlled via an input signal generated by the computer. Calibration of the source (figure 3.9) was required to determine the amount of power as a function of the DC control voltages. The laser was modulated with a DC signal ranging from 0V (full power) to 4.5V (off), with voltage steps of 50mV. The voltage generated by the photodiode current across a

resistance of 100Ω was measured. Laser power was then calculated assuming a flux responsivity of 0.50A/W (given by the manufacturer) and active area diameter of 100μm. A forth order polynomial curve was fitted to the data using the least squares method. The resulting equation is used to calculate the power and the energy for a given control voltage during the in vivo testing of the FLAMES

$$P = \frac{I}{R} \qquad \text{(Equ. 3.3)}$$

P: Power (mW)
I: Current (mA)
R: Responsivity mA/mW)

$$P(mW/mm^2) = \frac{P(mW)}{\frac{D^2(mm)\times\pi}{4}} \qquad \text{(Equ. 3.4)}$$

P: Power
D: diameter

$$E = P \times \frac{s}{10} \qquad \text{(Equ. 3.5)}$$

E: energy (mJ/cm^2)
P: power (mW/mm2)
s: pulse width (ms)

Figure 3.10 and 3.11 show the power and energy measurements. It is clear from the figures that the system output changes almost linearly.

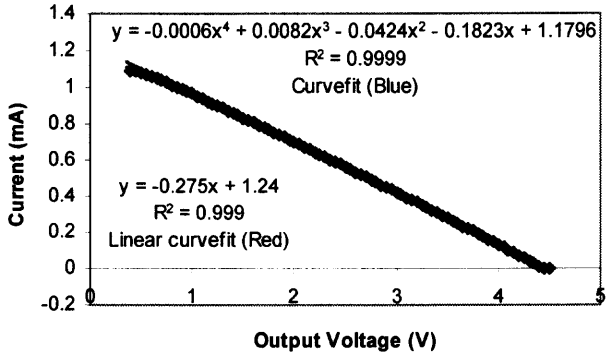

Figure 3.9 The Laser Calibration. Percent error in curve fit = 0.79.

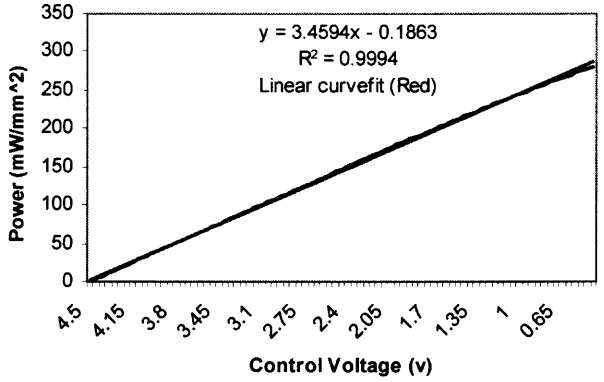

Figure 3.10 The power measurements.

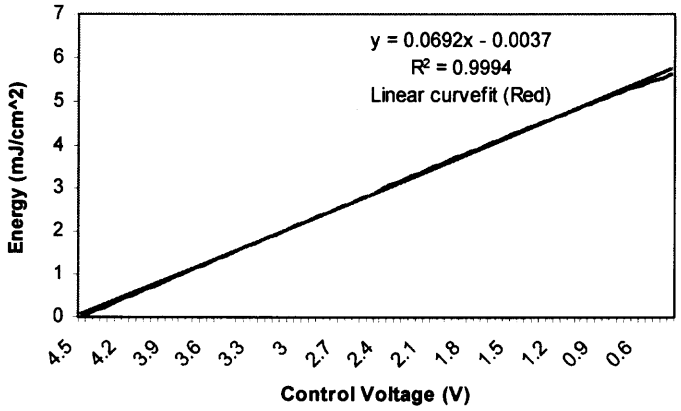

Figure 3.11 The energy measurements.

The laser profile has a Gaussian shape, where the maximum energy exists at the center. The Gaussian function is

$$f(x) = ae^{-(x-b)^2/c^2} \qquad \text{(Equ. 3.6)}$$

a: the amplitude
c: the standard deviation

The next step was to test if the profile of the NIR laser source is changed as a function of distance between the laser source and the surface of the active area of the photodiode. The profile was measured as follow; (1) we determine the center of the active area of the photodiode (a commercial photodiode was used that has 0.1 mm diameter) by determining the maximum voltage. The infrared light is not visible so a detector paper was used that converts the infrared to a visible light for localizing the beam. (2) We moved from the center in steps of 0.01, 0.05, and 0.1 mm toward the right and left side. Figures (3.12, 3.13, 3.14, 3.15, and 3.16) show the profiles at different distances (between the laser source and the surface of the photodiode). The curve-fitting of the laser profile was done on Matlab using (lsqcurvefit) function. It is obvious from the figures that the Gaussian shape of the profiles does not change as the distance between the laser and the photodiode change. Some profiles show better fit than others, but all of them are considered valid and have small error in the curve fit. The standard deviation (which is a measure of how much the curve spreads) has changed as a function of distance.

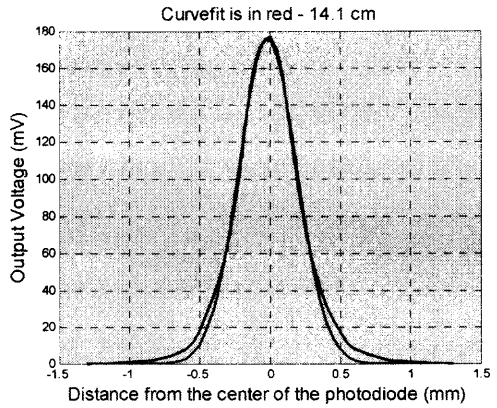

Figure 3.12 Laser profile at **14.1** cm distance between the laser and the photodiode surface. $y = 175.18\,e^{(-(x+0.0159)^2/0.29^2)}$. Percent error in curve fit = 4%.

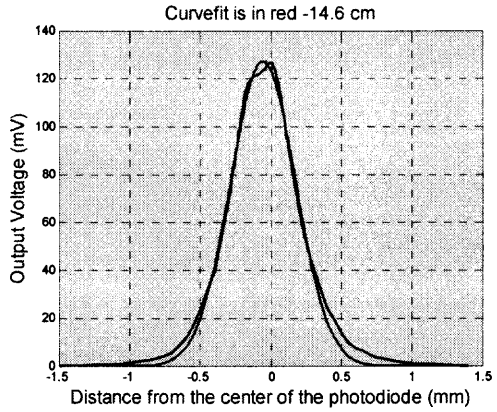

Figure 3.13 Laser profile at **14.6** cm distance between the laser and the photodiode surface. $y = 127.21e^{(-(x+0.056)^2/0.33^2)}$. Percent error in curve fit = 4.15%.

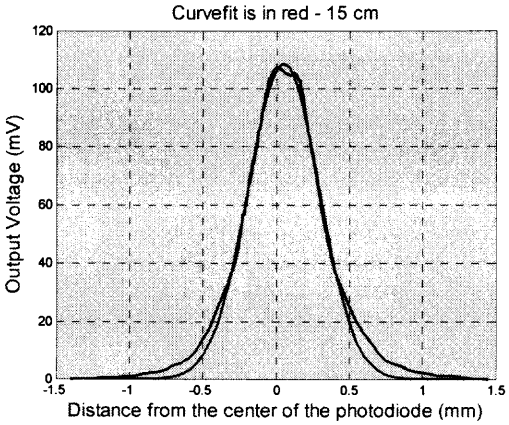

Figure 3.14 Laser profile at **15** cm distance between the laser and the photodiode surface. $y = 108.4e^{(-(x-0.05)^2/0.34^2)}$. Percent error in curve fit = 4.2%.

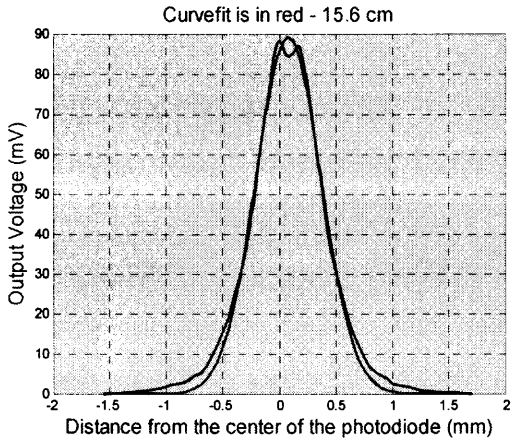

Figure 3.15 Laser profile at **15.6** cm distance between the laser and the photodiode surface. $y = 89.04e^{(-(x-0.081)^2/0.408^2)}$. Percent error in curve fit = 3.95%.

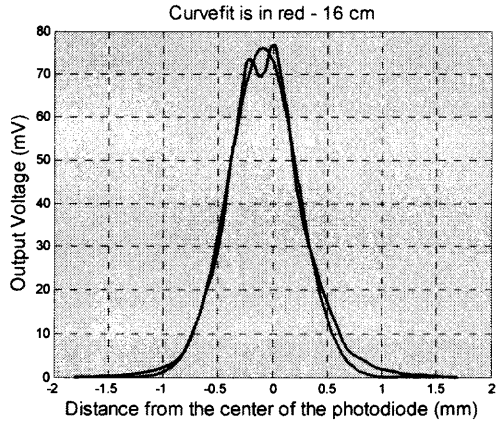

Figure 3.16 Laser profile at **16** cm distance between the laser and the photodiode surface. $y = 76.13e^{(-(x+0.09)^2/0.45^2)}$. Percent error in curve fit = 5.5%.

The next step was to make sure that the profiles do not change with changing the control voltages at certain distance (15 cm), so the profiles were measured with 0, 1, 2, 3, and 4 V as shown in figures (3.17, 3.18, 3.19, 3.20, and 3.21). The standard deviations of the curves at 1-4 voltages gave values close to the standard deviation at 15 cm (0.34); 0.35 at 1 V, 0.366 at 2 V, 0.37 at 3V, and 0.36 at 4 V. We can conclude from theses measurements that the profiles at 15 cm do not change with changing the control voltages.

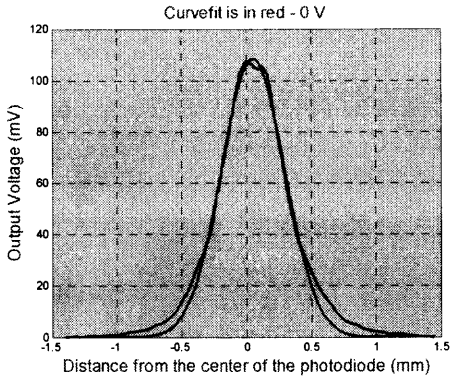

Figure 3.17 Laser profile at **15** cm distance between the laser and the photodiode surface and **0** V as control voltage. $y = 108.4e^{(-(x-0.05)^2/0.34^2)}$. Percent error in curve fit = 4.2%.

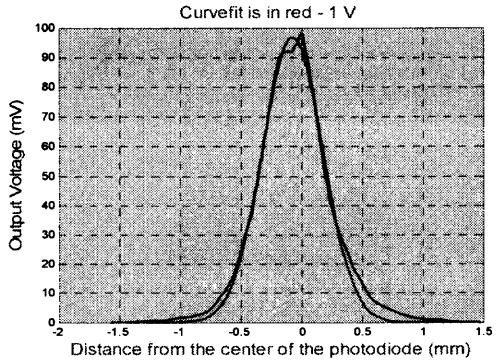

Figure 3.18 Laser profile at **15** cm distance between the laser and the photodiode surface and **1** V as control voltage. $y = 96.79e^{(-(x+0.073)^2/0.35^2)}$. Percent error in curve fit = 4.25%.

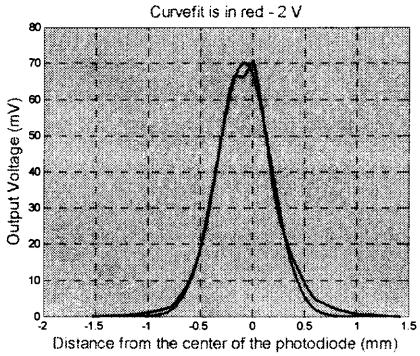

Figure 3.19 Laser profile at **15** cm distance between the laser and the photodiode surface and **2** V as control voltage. $y = 70.11e^{(-(x+0.079)^2/0.366^2)}$. Percent error in curve fit = 4.2%.

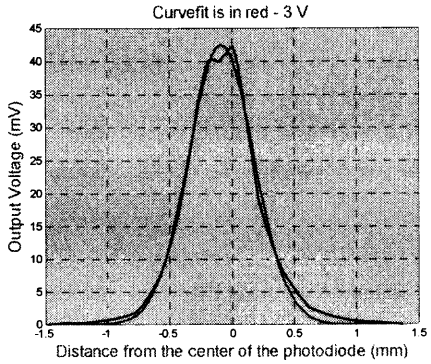

Figure 3.20 Laser profile at **15** cm distance between the laser and the photodiode surface and **3** V as control voltage. $y = 42.38e^{(-(x+0.0854)^2/0.37^2)}$. Percent error in curve fit = 4.22%.

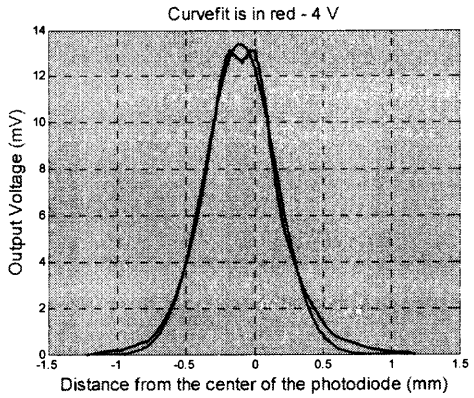

Figure 3.21 Laser profile at **15** cm distance between the laser and the photodiode surface and **4** V as control voltage. $y = 13.42e^{(-(x+0.104)^2/0.36^2)}$. Percent error in curve fit = 4.63%.

In the animal experiments a top plastic piece was used to clamp the nerve to a certain thickness (as shown in figure 3.24). So the final step of the laser calibration was to make sure that the profile does not change with using the plastic piece. Figure 3.22 shows the profile (at 15 cm) using a commercial photodiode with 0.08 mm diameter and without using the plastic piece. A standard deviation of 0.267 was obtained; this value is less than 0.34 because we are using a smaller diameter photodiode. Figure 3.23 shows the profile with using the plastic piece in top of the photodiode, the standard deviation was 0.26 which is almost the same value obtained without using the plastic piece. The two figures

show the Gaussian shape of the two profiles, and this implies that the profile does not change with using the plastic piece.

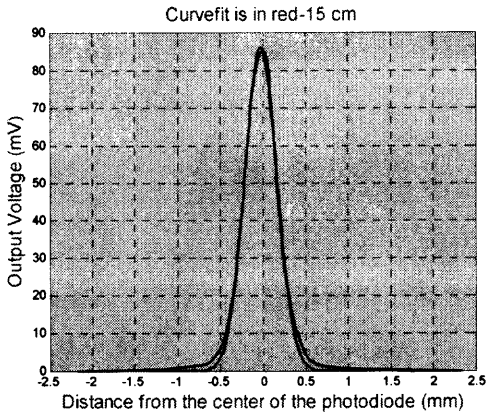

Figure 3.22 Laser profile at **15** cm distance between the laser and the photodiode surface. 0.08mm diameter photodiode. Without the plastic piece. $y = 85.85e^{(-(x+0.025)^2/0.267^2)}$. Percent error in curve fit = 2.88%.

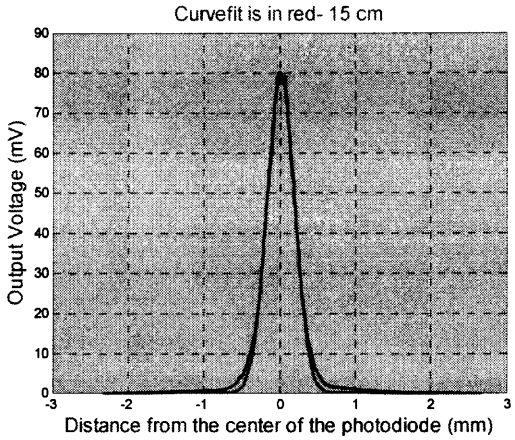

Figure 3.23 Laser profile at **15** cm distance between the laser and the photodiode surface. 0.08mm diameter photodiode. With the plastic piece. $y = 79.16e^{(-(x-0.0147)^2/0.26^2)}$. Percent error in curve fit = 2.98%.

3.3 NIR Transmittance and Penetration Depth in the Rat Peripheral Nerve:

This section deals with the transmitted light power measurements through the rat sciatic nerve. Penetration depth and reflectance calculations were obtained. We compared the rat sciatic nerve results with human brain white matter.

3.3.1 Methods:

Six Sprague-Dawley rats (400-500 g) were used for this study. The anesthesia was induced (50mg/kg) and maintained with sodium pentobarbital with further doses as needed. The body temperature was continuously monitored and maintained between 36-37°C using a temperature regulated heating pad. Tracheotomy was performed to connect the animal to a respirator. Respiration rate and end-tidal CO_2 were monitored. The sciatic nerves were dissected bilaterally and explanted. The epineurium and connective tissue were carefully removed with minimal stretching of the nerve in a Petri dish. The nerve was kept moist using saline solution at room temperature. All experimental procedures were approved by the Animal Care Committee at Rutgers University.

A commercial photodiode (G9842, circular active area, ø0.08mm, Hamamatsu, GaAs PIN photodiode) was used to measure the transmitted light power through the sciatic nerve. The photodiode was first secured at the bottom of a plastic apparatus with a channel that is 2mm wide and 0.5mm deep (Figure 3.24). The explanted rat sciatic nerve was then placed inside the channel, which then took the shape of the channel filling it wall-to-wall. Plastic pieces, transparent at NIR wavelengths, were placed over the nerve with varying heights from the photodiode plane and clamped securely. This set-up allowed us to control the length of the pathway precisely that the laser beam traveled

inside the neural tissue. The laser was centered above the set-up using a 3-axis micromanipulator and aimed at the photodiode's active area.

The transmittance of the nerve was obtained for a few different thicknesses of the nerve sample. The penetration depth (***a***) was estimated using a simple exponential curve fit through the data points according to Beer's law. When only two measurement points were available, the penetration depth was found using

$$a = \frac{(d2\text{-}d1)}{\ln(\frac{T1}{T2})} \qquad \text{(Equ. 3.7)}$$

where *d1* and *d2* are the neural tissue thicknesses and *T1* and *T2* are the transmittances measured at *d1* and *d2* respectively. The reflectance (***R***) was found by substituting the calculated penetration depth back in Equ. 1.

$$R = (1 - (\frac{T1}{I_0}))e^{\frac{d1}{a}} \qquad \text{(Equ. 3.8)}$$

The incident light power (*Io)* is measured with no neural tissue present. The horizontal extent of the tissue sample perpendicular to the light beam was assumed to be sufficiently large to neglect the boundary effects. The laser source (DLS-500-830FS-100, StockerYale, Canada) was a 74mW, 830nm semiconductor source with a circular beam shape that had a Gaussian intensity with a standard deviation of about 260μm at the surface of the tissue slab. The laser was placed 15cm from the tissue surface.

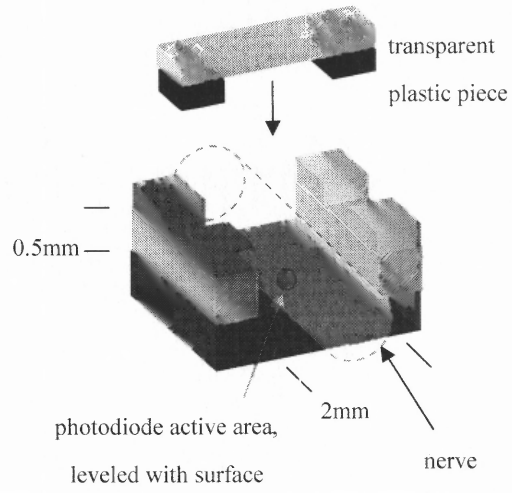

Figure 3.24 Preparation used to measure the penetration depth in the rat sciatic nerve.

3.3.2 Results and Discussion:

Two point measurements (thickness of 0.55mm and 1.1mm) were made on the first five samples and three point measurements (0.52, 0.89, and 1.07mm) on the remaining two samples. Figure 3.25 shows the transmittance values measured from seven samples as a function of nerve sample thickness. The exponential line is a curve fit to the mean values. The mean transmittance was 25.1±0.96%, 19.6±3.48%, 7.19±0.26%, 4.79±0.22%, and 4.22±0.61% at thickness values of 0.52, 0.55, 0.89, 1.07, and 1.1mm respectively.

The calculated penetration depth had a mean of 0.35mm with a standard deviation of 0.023mm. The reflectance measurements varied substantially between the samples with a mean value of 4.7% and a standard deviation of 20%.

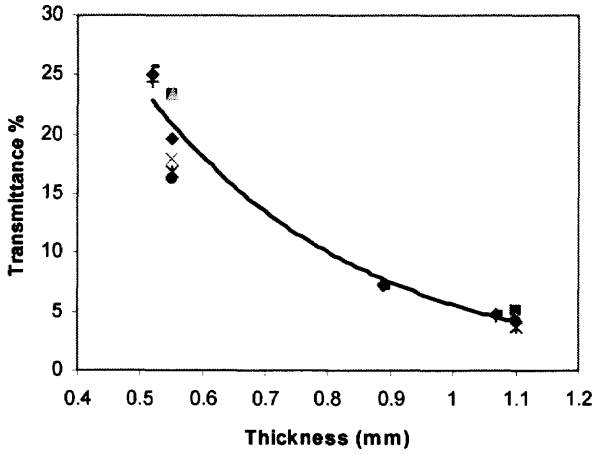

Figure 3.25 The transmittance of seven samples as a function of the rat sciatic nerve thickness. The exponential curve is the fit to the mean values shown in diamonds (♦) and each symbol type indicates a different tissue sample.

In our study, we are using the same principle that Eggert and Blazek group used (explained earlier). They evaluated the penetration depth according to Beer's law by experimentally measuring the transmittance and the reflectance at one point measurement. On the other hand, we evaluated the penetration depth by only measuring the transmittance experimentally but at more than one point measurement.

As mentioned in the literature, the tissue layer should be very thin in order to neglect the multiple scattering. In our work, we are using 0.5-1mm thicknesses, which is the same range of thickness that Eggert and Blazek group used. Using large thicknesses is one of the shortcomings of our technique and this is obvious in the reflectance calculations. The reflectance results were not consistent, and some results were negative. "Scattering is usually caused by random spatial variations in tissue density, refractive index, and dielectric constant, and actual light distribution can be substantially different from distribution estimated using Beer's law" [24]. For example, backscattering can cause the light fluence rate to be higher than the total light at zero thickness. And this

explains the inconsistency in our reflectance calculations and obtaining negative results.

On the other hand, penetration depth calculations were consistent. The transmittance values measured followed the exponential behavior that governed by Beer's law as light propagate inside the tissue with high correlation (>0.98) in the exponential curve fit of each sample. Since we used large thicknesses, the calculated penetration depth varies from the penetration depth governed by Beer's law. However, this variance is not large because we obtained a high correlation in the curvefit.

Transmittance measurements demonstrated that FLAMES are feasible for implantation depths of as much as 1.1mm for the rat peripheral nerve that at this depth 4.22% of the incident light was transmitted. Since our reflectance calculations were not accurate, we were not able to exactly measure how deep the FLAMES can be implanted into the sciatic nerve and still be activated.

The measured penetration depth of the rat sciatic nerve is much smaller than the human white matter of the brain, which was measured as 2.3mm by Roggan *et al.* at 850 nm [23], 0.9mm by Yaroslavsky *et al.* at 850 nm) [15], and 0.75mm by Eggert *et al.* for the entire near infrared spectral range) [20].

The discrepancy in penetration depth of rat sciatic nerve and human white brain matter is due to the fact that there are differences in (1) the optical properties between tissues in rat and human, (2) the optical properties between white brain matter and peripheral nerve, and (3) the sample preparation techniques. As mentioned, there are differences in the white brain matter penetration depth results from group to another because each group uses different measurement techniques and different theoretical approaches.

Sample preparation techniques play a vital role in measurement of the tissue optical properties. In this study, the measurements were made immediately after removing the nerve from the rats. Because of the practical limitation of *in vivo* measurements we chose to do the measurements on the explanted nerves. For instance, the excessive connective tissue and the vascularization around the nerve made the measurements unstable. Reports in literature suggest that *in vitro* measurement of optical properties can adequately match the *in vivo* case [15]. In our work, the explanted nerves were not frozen or subjected to any fixation procedure.

3.4 NIR Transmittance and Penetration depth in the Rat Brain Cortex:

Rat brain cortex was investigated in this study. Penetration depth and reflectance calculations were obtained by measuring the transmittance of the brain sample at various thicknesses. The brain cortex has two different matters; grey matter and white matter. As explained in the literature, there are variations in the optical properties between the white matter and the grey matter. The grey matter has a higher penetration depth than the white matter.

3.4.1 Methods:

Three Sprague-Dawley rats (400-500 g) were used for this study. The anesthesia was induced (50mg/kg) and maintained with sodium pentobarbital with further doses as needed. The body temperature was continuously monitored and maintained between 36-37°C using a temperature regulated heating pad. The brain cortex was dissected and explanted. Since the brain cortex samples were soft, the samples were placed in 10%

formalin and kept in refrigerator for 24 hours to be fixed. The white and grey matters were dissected and separated. The same setup and measurement techniques explained in figure 3.24 were used. All experimental procedures were approved by the Animal Care Committee at Rutgers University.

3.4.2 Results and Discussion:

Three point measurements (thickness of 0.52, 0.89, and 1.07mm) were made on the first sample and four point measurements (0.52, 0.65, 0.78, and 1.07mm) on the remaining four samples for both grey and white brain matter.

Figure 3.26 shows the transmittance values measured from five samples as a function of grey brain matter sample thickness. The exponential line is a curve fit to the mean values. The mean transmittance was 45.76±4.57%, 35.24±3.61%, 24.13±11.13%, 15.6%, and 11.97±15.1% at thickness values of 0.52, 0.65, 0.78, 0.89, and 1.07mm respectively. The calculated penetration depth of the grey brain matter samples had a mean of 0.41mm with a standard deviation of 0.026mm. The reflectance calculations were not accurate, that negative reflectance values were obtained from the rat brain grey matter.

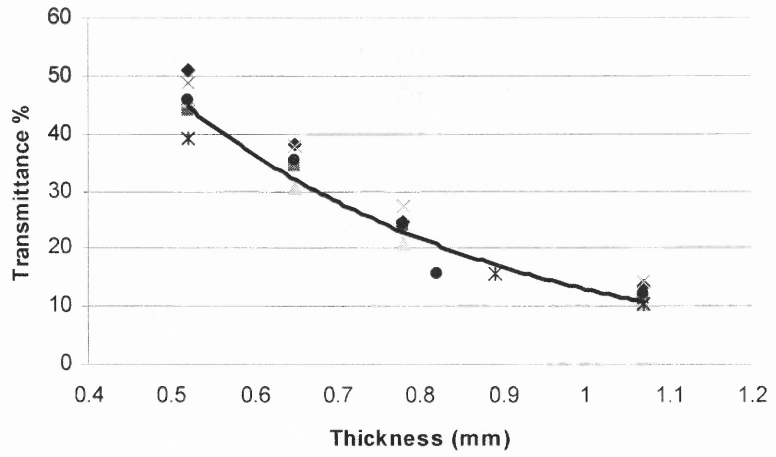

Figure 3.26 The transmittance of five samples as a function of the rat grey brain matter thickness. The exponential curve is the fit to the mean values shown in diamonds (♦) and each symbol type indicates a different tissue sample.

Figure 3.27 shows the transmittance values measured from five samples as a function of white brain matter sample thickness. The exponential line is a curve fit to the mean values. The mean transmittance was 16.63±38.83%, 10.36±21.1%, 6.02±7.29%, 8.71%, and 3.65±42.18% at thickness values of 0.52, 0.65, 0.78, 0.89, and 1.07mm respectively. The calculated penetration depth of the white brain matter samples had a mean of 0.355mm with a standard deviation of 0.023mm. The reflectance measurements varied substantially between the samples with a mean value of. 28.4% and a standard deviation of 25%.

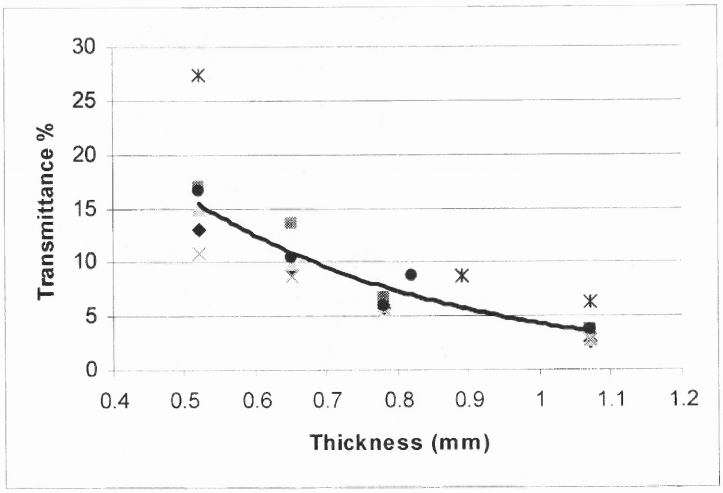

Figure 3.27 The transmittance of five samples as a function of the rat white brain matter thickness. The exponential curve is the fit to the mean values shown in diamonds (♦) and each symbol type indicates a different tissue sample.

Penetration depth calculations also were consistent for both grey and white brain matter. The transmittance values measured followed the exponential behavior with high correlation (>0.99) in the exponential curve fit of each grey brain matter sample. The white brain matter samples had a correlation greater than 0.98 except in one sample (0.95 correlation). Also in the rat brain cortex measurements, the variance of our calculated penetration depth from Beer's law is not large because we obtained a high correlation in the curvefit.

The measured penetration depth of the rat brain white matter is much smaller than the human brain white matter. The penetration depth as well as the transmittance in the rat grey brain matter is higher than that in the white brain matter, but the difference in the transmittance between the grey and white matter is much significant than the difference in the penetration depth. Although the reflectance calculations were not accurate, but it can be concluded that grey matter reflectance is much higher than that of white brain matter. And therefore, the transmittance in the grey matter is much higher. On the other

hand, we expected the difference in the penetration depth between the grey and white matter to be higher (0.41mm to 0.355mm) because the difference in the transmittance is very significant. The reflectance results for both grey and white brain matter were not very consistent because of the multiple backscattering effects.

Transmittance measurements demonstrated that FLAMES are feasible for implantation depths of as much as 1.07mm for rat brain cortex. Since the transmitted light power through rat brain gray matter was much higher than that of the white matter and the sciatic nerve, FLAMES can be implanted into the rat brain gray matter and still be activated for larger implementation depths and much further than 1.07mm.

3.5 Conclusion

The results suggest that FLAMES approach is feasible for implantation depths of a few millimeters in the peripheral and central nervous system. The transmitted light power through rat brain gray matter was much higher than that of the white matter and the sciatic nerve. Penetration depth is a good indicator to the attenuation of the light while traveling through an object.

APPENDIX A

THE MATLAB CODE USED FOR CURVE FITTING

This m-file does curve fitting to the data.

On one file:

```
xdata = tissue(:,1);          % Distance
ydata = tissue(:,2);          % voltage (mV)
X0=[ 17.8708 1.0828e-008  0.4298];

OPTIONS=optimset('TolX',1e-10, 'TolFun', 1e-10, 'MaxFunEvals', 1000);
[R,RESNORM,RESIDUAL,EXITFLAG,OUTPUT] = lsqcurvefit(@model, X0, xdata,
ydata,[],[],OPTIONS) ;
R(1)
R(2)
R(3)
EXITFLAG
OUTPUT

YDATA=model(R,xdata);

figure
plot(xdata,ydata)
hold
plot(xdata,YDATA,'r')
title('curvefit is in red')
hold
```

On another file:

```
function F =  model(R,xdata)
 a=R(1);
 b=R(2);
 c=R(3);



        F = a .* exp ( -1.* ((xdata-b).^2)/ c.^2); %Gaussian function
 end
```

APPENDIX B

THE MATLAB CODE USED FOR PENETRATION DEPTH AND REFLECTANCE CALCULATIONS

This m-file calculates the penetration depth and the reflection at the surface from transmission measurements at two different thicknesses of the neural tissue.

```
T1=[7.6, 7.89, 11.8, 15.9, 17.5];    % tranmission through d1, unit same
as Iin, using R1
T2=[18.7, 17.2, 25.2, 30.5 39.4];    % transmission through d2, using R2
Iin=[49.6, 49.6, 65, 68.5, 80];;    % incident light in arbitrary units

d1=0.55;      %mm
d2=1.1;       %mm
R1=98.2;     % resistor in Ohms
R2=997;      % resistor in Ohms

Iin=Iin/R1;
T1=T1/R1;
T2=T2/R2;

a=(d2-d1)./log(T1./T2)      % penetration depth
Ref=100*((ones(1,5)-(T1*1/0.93950762./Iin)).*exp(d1./a))   %reflectance
in percentages

mean_a=mean(a)
std_a=std(a)

mean_Ref=mean(Ref)
std_Ref=std(Ref)
```

REFERENCES

1. Boggs J.W., B.J. Wenzel, K.J. Gustafson, and W.M. Grill, "Emptying by Intermittent Stimulation of the Pudendal Nerve," J Neural Eng. 3:1, 43-51, 2006.

2. Muthuswamy J., M. Okandan, A. Gilletti, M.S. Baker, and T. Jain, "An Array of Microactuated Microelectrodes for Monitoring Single-neuronal Activity in Rodents," IEEE Trans Biomed Eng. 52(8): 1470-1477. Aug. 2005.

3. Loeb G.E., Peck R.A., Moore W.H., and Hood K., "BION System for Distributed Neural Prosthetic Interfaces," Med Eng Phys 23:1, 9-18, 2001.

4. D.M. Zhou, and R. J. Greenberg, "Electrochemical Characterization of Titanium Nitride Micro Electrode Arrays for Charge-injection Applications," Proceedings of the 2th Annual International Conference of the IEEE EMBS Cancun, Mexico. September 17-21.2003.

5. James D. Weiland, David J. Anderson, and Mark S. Humayun, "In Vitro Electrical Properties for Iridium Oxide versus Titanium Nitride Stimulating Electrodes," IEEE Trans Biomed Eng., Vol. 49, NO. 12, December 2002.

6. Andy Hung, David Zhou, Robert Greenberg, and Jack W. Judy, "Dynamic Electrochemical Stimulation of Micromachined Electrodes for Neural-stimulation Systems," Proceedings of the 1 st International IEEE EMBS, Conference on Neural Engineering, Capri Island, Italy March 20-22, 2003.

7. Stuart F. Cogan. "Microelectrode Coatings for Neural Stimulation and Recording," Proceedings of the 25th Annual International Conference of the IEEE EMBS Cancun, Mexico. September 17-21,2003.

8. Stuart F. Cogan, Philip R. Troyk, Julia Ehrlich, Timothy D. Plante, and David E. Detlefsen, "Potential-biased, Asymmetric Waveforms for Charge-injection with Activated Iridium Oxide (AIROF) Neural Stimulation Electrodes," IEEE Trans Biomed Eng., VOL. 53, NO. 2, February 2006.

9. S. F. Cogan, T. D. Plante, and J. Ehrlich, "Sputtered Iridium Oxide Films (SIROFs) for Low-impedance Neural Stimulation and Recording Electrodes," Proceedings of the 26th Annual International Conference of the IEEE EMBS San Francisco, CA, USA • September 1-5, 2004.

10. Stuart F. Cogan, Philip R. Troyk, Julia Ehrlich, and Timothy D. Plante, "In Vitro Comparison of the Charge-injection Limits of Activated Iridium Oxide (AIROF) and Platinum-iridium Microelectrodes," IEEE Trans Biomed Eng., Vol. 52, NO. 9, September 2005.

11. http://en.wikipedia.org/wiki/Beer-Lambert_law, Feb 2007.

12. H.R. Eggert, and V. Blazek, "Optical Properties of Normal Human Intracranial Tissues in the Spectral Range of 400 TO 2500 nm," Optical Imaging of Brain Function and Metabolism, Edited by U. Dirnagel et al., Plenum Press, New York, 1993.

13. Frederick W. Koehler, Eunah Lee, Linda H. Kidder, and E. Neil Lewis, "Near Infrared Spectroscopy: the Practical Chemical Imaging Solution," Spectroscopy Europe 14/3 (2002).

14. Z. Amin, J. J. Donald, A. Masters, R. Kant, A. C. Steger, S. G. Bown, and W. R. Lees, "Hepatic Metastases: Interstitial Laser Photocoagulation with Real-time US Monitoring and Dynamic CT Evaluation of Treatment," Radiology, Vol 187, 339-347, 1993.

15. A.N. Yaroslavsky, P.C. Schulze, I.V.Y. Yaroslavsky, R. Schober, F. Ulrich, and H-J Schwarzmaier, "Optical Properties of Selected Native and Coagulated Human Brain Tissues in Vitro in the Visible and Near Infrared Spectral Range," Phys. Med. Biol. 47 (2002) 2059-2073.

16. Rune W. Berg, and David Kleinfeld, "Vibrissa Movement Elicited by Rhythmic Electrical Microstimulation to Motor Cortex in the Aroused Rat Mimics Exploratory Whisking," J Neurophysiol 90: 2950–2963, 2003.

17. Kimberlyn Gray, and M. Sahin, "Floating Light Activated Micro-Electrical Simulators," 35th Neural Interface Workshop, Bethesda, MD, Sep 2004.

18. http://en.wikipedia.org/wiki/Near_infrared_spectroscopy, Feb 2007.

19. Harsha Radhakrishnan, Arun Senapati, Dheerendra Kashyap, Yuan Bo Peng, and Hanli Liu. "Light Scattering from Rat Nervous System Measured Intraopertively by Near-infrared Reflectance Spectroscopy," Journal of Biomedical Optics 10(5), 051405 (September/October 2005).

20. Hans R. Eggert, and V. Blazek, "Optical Properties of Human Brain Tissue, Meninges, and Brain Tumors in the Spectral Range of 200 to 900 nm," Neurosurgery, Vol. 21, No. 4, 1987.

21. Lars O. Svaasand, and Reinold Ellingsen, "Optical Properties of Human Brain," Photochemistry and Photobiology, Vol. 38. No. 3. pp. 293-299, 1983

22. H.J.C.M. Sterenborg, M.J.C. Van Gemert, W. Kamphorst, J.G. Wolbers , W. Hogervorst, "The Spectral Dependence of the Optical Properties of Human Brain," Lasers in Medical Science Vol4:221 1989.

23. A. Roggan, O. Minet, C. Schroder, G. Muller, "The Determination of Optical Tissue Properties with Double Integrating Sphere Technique and Monte Carlo Simulations," SPIE Vol. 2100 Cell and Biotissue Optics (1994).

24. Ashley J. Welch, and Martin J.C. van Gemert, "Optical-Thermal Response of Laser-Irradiated Tissue," Lasers, Photonics, and Electro-optics (1995).

25. Frederick W. Koehler IV, Eunah Lee, Linda H. Kidder, and E. Neil Lewis, "Near Infrared Spectroscopy: the Practical Chemical Imaging Solution," Spectroscopy Europe 14/3 (2002).

26. Z. Amin, J. J. Donald, A. Masters, R. Kant, A. C. Steger, S. G. Bown, and W. R. Lees, "Hepatic Metastases: Interstitial Laser Photocoagulation with Real-time US Monitoring and Dynamic CT Evaluation of Treatment," Radiology, Vol 187, 339-347, 1993.

27. M. Johns, "Optical Properties of Living Tissues Determined in Vivo Using a Thin Fiber Optic Probe," PhD Dissertation, University of Texas at Arlington (2003).

28. P van der Zee, "Measurements and Molding of the Optical Properties of Human Tissue in the Near Infrared," PhD Dissertation, University of London (1992).

29. Christoph-Thomas Germer, Andre´ Roggan, Joerg P. Ritz, Christoph Isbert, Dirk Albrecht, Gerhard Muller, and Heinz J. Buhr, "Optical Properties of Native and Coagulated Human Liver Tissue and Liver Metastases in the Near Infrared Range," Lasers in Surgery and Medicine 23:194–203 (1998).

30. Joerg-P. Ritz, Andre Roggan, Christoph Isbert, Gerhard MuÈller, Heinz J. Buhr, and Christoph-T. Germer, "Optical Properties of Native and Coagulated Porcine Liver Tissue between 400 and 2400 nm," Lasers in Surgery and Medicine 23:194–203 (2001).

31. Ramtin Agah, A. H. Gandjbakhche, Massoud Motamedi, Ralph Nossal, and R. F. Bonner, "Dynamics of Temperature Dependent Optical Properties of Tissue: Dependence on Thermally Induced Alteration," IEEE Trans Biomed Eng. VOL. 43, NO. 8, Aug 1996.

32. Frederic Bevilacqua, Dominique Piguet, Pierre Marquet, Jeffrey D. Gross, Bruce J. Tromberg, and Christian Depeursinge, "In Vivo Local Determination of Tissue Optical Properties: Applications to Human Brain," 1 August 1999 / Vol. 38, No. 22 / Applied Optics.

33. Maureen Johns, Cole A. Giller, Dwight C. German, and Hanli Liu, "Determination of Reduced Scattering Coefficient of Biological Tissue from a Needle-like Probe," 27 June 2005 / Vol. 13, No. 13 / Optics Express 4828.

34. Arun Kumar Senapati, Harsha Radhakrishnan, Hanli Liu, and Yuan Bo Peng, "Detection of Degeneration in Rat Sciatic Nerve by in Vivo Near Infrared Spectroscopy" Brain Research Protocols 14 (2005) 119–125.

35. D T Delpy, m Cope, P van der Zee, S Arridge, Susan Wary, and J Wyatt, "Estimation of Optical Pathlength through Tissue from Direct Time of Flight Measurement". Phys. Med. Biol., 1988 Vol. 33, No 12, 1433-1442.

36. http://en.wikipedia.org/wiki/Spectrometry, Feb 2007.

37. Michael S. Patterson, B. Chance, and B. C. Wilson, "Time Resolved Reflectance and Transmittance for the Noninvasive Measurement of Tissue Optical Properties". 15 June 1989 / Vol. 28, No. 12 / Applied Optics.

38. American National Standards Institute. American National Standard for Safe Use of Lasers. New York: American National Standards Institute, 1993.

39. Oshiro T., and R. G. Calderhead, "Low Level Laser Therapy: A Practical Introduction," New York: Wiley, 1988.

40. John G, and Webster, "Medical Instrumentation Application and Design" 3rd edition, John Wiley & Sons Co., Inc. (1998).

41. A. Norlin, J. Pan, and C. Leygrafa, "Investigation of Electrochemical Behavior of Stimulation /Sensing Materials for Pacemaker Electrode Applications," Journal of the Electrochemical Society (2005).

42. Cameron T., Liinamaa T. L., G. E. Loeb, and F. J. R. Richmond, "Long-term Biocompatibility of a Miniature Stimulator Implanted in Feline Hind Limb Muscles" IEEE Trans Biomed Eng. 45:1024-35, 1998.

43. Choi C T M, L. Wei-Dian Lai, and Yu-Bin Chen, "Comparison of the Electrical Stimulation Performance of Four Cochlear Implant Electrodes" IEEE Trans Magn. 41(5): 920-23, May 2005.

44. Goto K., T. Nakagawa, O. Nakamura, and S. Kawata, "An Implantable Power Supply with an Optically Rechargeable Lithium Battery," IEEE Trans Biomed Eng, 48(7):830-33, 2001.

45. Haueisen J., C. Ramon, P. Czapski, and M. Eiselt, "On the Influence of Volume Currents and Extended Sources on Neuromagnetic Fields: a Stimulation Study," Ann. Biomed. Eng., 23:728-39, 1995.

46. Liu, X., D. B. McCreery, L. A. Bullara, and W. F. Agnew, "Evaluation of the Stability of Intracortical Microelectrode Arrays," IEEE Trans Neural Syst Rehabil Eng. 14(1):91-100, June 2006.

47. Lyons G.M., T. Sinkjaer, J. H. Burridge, and J. D. Wilcox, "A Review of Portable FES-based Neural Orthoses for the Correction of Drop Foot," IEEE Trans Neural Syst Rehabil Eng. 10(4): 260– 279, Dec. 2002.

48. Peyman G., A. Y. Chow, C. Liang, V. W. Chow, J. I. Perlman, and N. S. Peachey, "Subretinal Semiconductor Microphotodiode Array," Ophthalmic Surg. Lasers 29(3): 234-41, 1998.

49. Vetter, R.J., J. C. Williams, J. F. Hetke, E. A. Nunamaker, and D. R. Kipke. Chronic neural recording using silicon-substrate microelectrode arrays implanted in cerebral cortex. IEEE Trans Biomed Eng. 51(6): 896 – 904, June 2004.